Optimizing a Human Monoclonal Antibody for Better Neutralization of SARS-CoV-2

Qian Wang[1,2,3,9], Yicheng Guo[1,3,9], Ryan G. Casner[4,5,6,9], Jian Yu[1], Manoj S. Nair[1], Jerren Ho[1], Eswar R. Reddem[4,5], Chih Chen Tzang[1], Yaoxing Huang[1,2,3], Lawrence Shapiro[1,4,5,*], Lihong Liu[1,3,7*], David D. Ho[1,2,3,8,10,*]

[1]Aaron Diamond AIDS Research Center, Columbia University Vagelos College of Physicians and Surgeons, New York, NY 10032, USA

[2]Pandemic Research Alliance unit at the Wu Center for Pandemic Research, Columbia University Vagelos College of Physicians and Surgeons, New York, NY 10032, USA

[3]Division of Infectious Diseases, Department of Medicine, Columbia University Vagelos College of Physicians and Surgeons, New York, NY 10032, USA

[4]Zuckerman Mind Brain Behavior Institute, Columbia University, New York, NY 10027, USA

[5]Department of Biochemistry and Molecular Biophysics, Columbia University Vagelos College of Physicians and Surgeons, New York, NY 10032, USA

[6]Current address: Large Molecules Research, Sanofi R&D, Cambridge, MA 02141, USA

[7]Current address: State Key Laboratory of Virology and Taikang Center for Life and Medical Sciences, Wuhan University, Wuhan, Hubei, 430072, China

[8]Department of Microbiology and Immunology, Columbia University Vagelos College of Physicians and Surgeons, New York, NY 10032, USA

[9]These authors contributed equally

[10]Lead contact

*Correspondence: lss8@cumc.columbia.edu (L.S.), ll3411@cumc.columbia.edu, (L.L.), dh2994@cumc.columbia.edu (D.D.H.)

SUMMARY

SARS-CoV-2 has largely evolved to resist antibody pressure, with each successive viral variant becoming more and more resistant to serum antibodies in the population. This evolution has rendered inactive all therapeutic monoclonal antibodies previously authorized, and it is now threatening the remaining clinical product for immunoprophylaxis against COVID-19. We report herein the isolation of a human monoclonal antibody with a broad but incomplete SARS-CoV-2 neutralization profile, but structural analyses and mutational scanning led to the engineering of variants that resulted in greater antibody flexibility while binding to the viral spike. Three such optimized monoclonal antibodies neutralized all SARS-CoV-2 strains tested with much improved potency and breadth, including against subvariants KP.3.1.1 and XEC that are dominant today. The findings of this study not only present new antibody candidates for clinical development against COVID-19, but also introduce a unique engineering approach to improve antibody activity via increasing conformational flexibility.

Keywords: SARS-CoV-2, COVID-19, JN.1, KP.3.1.1, XEC, monoclonal antibodies, antibody engineering, virus neutralization, viral evolution, mutational scanning, conformational flexibility, VH3-53, cryo-EM, and escape mutations.

INTRODUCTION

Since the emergence of COVID-19 in late 2019, its causative agent, SARS-CoV-2, has undergone considerable evolution driven by immune pressure, with each successive viral variant becoming more resistant to serum antibodies elicited by prior infection and/or vaccination. By late 2020, mutations in the viral spike protein resulted in a discernible antigenic drift that yielded the Alpha variant, which evaded antibodies targeting the antigenic supersite on the N-terminal domain (NTD)[1-3]. Shortly thereafter, further antigenic drift led to the Beta and Gamma variants that evaded not only NTD-directed antibodies but also some antibodies directed to so-called class 1 and class 2 regions of the receptor-binding domain (RBD)[1,4,5]. These variants were in turn rapidly replaced by the Delta variant that dominated much of 2021, and it evaded antibodies directed to select class 2 and class 3 epitopes on the RBD[6]. Importantly, this initial wave of SARS-CoV-2 variants knocked out three therapeutic monoclonal antibodies (mAbs) authorized to treat COVID-19 infection – etesevimab, bamlanivimab, and casirvimab[6-10].

The first major SARS-CoV-2 antigenic shift occurred with emergence of the Omicron (BA.1) variant in late 2021 in southern Africa[11,12], likely due to a saltatory event resulting in an accumulation of 34 spike mutations. This variant rapidly gain dominance in the population, as a consequence of its exceptional resistance to serum antibodies in the population[13-18]. Specifically, mutations in Omicron impaired the neutralizing activity of antibodies targeting all regions (classes 1-4) of the RBD, as well as two additional clinically authorized mAbs – imdevimab and tixagevimab[9,13,19]. Antigenic drift from BA.1 then ensued successively throughout 2022 and yielded subvariants BA.2, BA.5, and BQ.1.1, each being more antibody resistant than its predecessor. This evolutionary drift also knocked out the utility of three more clinically authorized mAbs – sotrovimab, ciligavimab, and bebtelovimab[19-23].

The second major antigenic shift was detected in late 2022 when a recombination event between BA.2 and BA.2.75 resulted in the XBB subvariant, which promptly evolved into XBB.1.5, EG.5.1, HK.3, and HV.1 via further antigenic drift[11,24-26]. Again, each progeny subvariant was more antibody resistant than its predecessor, largely by evading more antibodies directed to the class 1 region of RBD. Sequentially, these subvariants dominated much of 2023 until the third major antigenic shift led to the emergence of BA.2.86, which presumably was due to another saltatory event, again in southern Africa, leading to an accumulation of >30 mutations in the BA.2 spike[27]. This new subvariant was again highly resistant to serum neutralizing antibodies, including those targeting the subdomain 1 (SD-1) region of spike[28-30]. With one additional spike mutation, L455S, BA.2.86 became JN.1 that has since gained dominance worldwide from late 2023 until recently[31,32].

In March of this year, a monoclonal antibody known as pemivibart (Permagard or VYD222) was authorized for clinical use as pre-exposure prophylaxis for immunocompromised individuals who do not respond robustly to COVID-19 vaccines[33]. This antibody was specifically engineered to have broad activity against many known SARS-CoV-2 strains, including JN.1. However, as the JN.1 sublineage continued its antigenic drift, new forms such

as KP.2 and KP.3 began to replace their predecessor in recent months. Currently, the dominant SARS-CoV-2 is KP.3.1.1, and the emergent XEC is steadily gaining ground[34]. Alarmingly, these subvariants are already ~18-28-fold more resistant to pemivibart in vitro than JN.1[35]. This looming threat to the only authorized pre-exposure prophylaxis for millions of immunocompromised individuals who live in fear of COVID-19 is a stark reminder of the necessity to continue to develop more medical interventions to keep up with SARS-CoV-2 evolution.

We now describe the isolation and characterization of a human monoclonal antibody, 19-77, with a broad but incomplete SARS-CoV-2 neutralization profile. Structural analyses and mutational scanning led to the construction of engineered antibody variants, 19-77Δ, with a single amino-acid substitution at residue R71 in the framework region 3 of the heavy chain. These modifications resulted in greater flexibility of the complementarity-determining regions (CDRs) of the heavy chain while binding to the viral spike, thereby enabling three 19-77Δ variants to neutralize all SARS-CoV-2 strains tested with much improved potency and breadth, including against the prevalent JN.1 sublineages today. The findings of this study not only offer new antibody candidates for pre-exposure prophylaxis against COVID-19 for immunocompromised individuals, but also introduce a unique engineering approach to improve antibody activity.

RESULTS

Isolation and characterization of mAb 19-77

To isolate new neutralizing mAbs against SARS-CoV-2, we studied Donor 19 who had been infected by the Omicron BA.5 subvariant despite having received three doses of the original monovalent vaccine (BNT162b2) and one dose of the WT/BA.5 bivalent vaccine (mRNA-1273.222) (**Figure S1A**). His serum, obtained ~7 months after breakthrough infection, strongly neutralized the D614G strain but less potently against XBB.1.5 and SARS-CoV (**Figure S1B**). Given the dominance of XBB.1.5 at the start of this study, XBB.1.5 and SARS-CoV spikes were used as probes to sort antigen-specific memory B cells from his peripheral blood mononuclear cells (PBMCs). The proportions of his antigen-specific B cells were 0.16% for XBB.1.5 spike, 0.067% for SARS-CoV, and 0.12% for both XBB.1.5 and SARS-CoV spikes; in contrast, PBMCs from two healthy donors showed negligible antigen-specific B cells (**Figure S1C**).

Donor 19's memory B cells from quadrants 2 and 3 (**Figure S1C**) were then subjected to single-cell RNA sequencing using 10X Genomics to obtain paired heavy and light chain sequences of each B cell receptor, as previously described[36]. A total of 113 paired sequences were selected, and the corresponding antibodies were synthesized for in vitro characterization. A majority (75) of the mAbs bound the D614G spike at a concentration of 10 μg/ml (data not

shown), but only 29 neutralized either D614G or EG.5.1 in vitro (**Figure S1D**). Among the neutralizing mAbs, 19-77 was chosen for further studies, because it not only bound strongly to the D614G spike and RBD by immunoassays (**Figure 1A**), but also showed broadly neutralizing activity against many SARS-CoV-2 strains (**Figure 1B**). Specifically, in pseudovirus assays, 19-77 neutralized D614G, Alpha, Beta, Gamma, Delta, BA.1, BA.2, BA.5, BQ.1.1, XBB.1.5, EG.5.1, BA.2.86, and JN.1 with IC_{50} values <0.05 μg/ml. However, its neutralizing activity was lower against HK.3 and JF.1, and not detectable against JD.1.1 or SARS-CoV.

Genetic analysis revealed that the heavy chain of 19-77 utilized IGHV3-53 (**Figure S1E**), showing that this antibody belonged to the well-studied VH3-53/66 class of antibodies targeting the SARS-CoV-2 spike. Its light chain originated from IGKV3-11. Notably, the CDRH3 of 19-77 contained only 9 amino acids, one of the shortest among published VH3-53/66 class mAbs (**Figure 1C**). Moreover, the level of somatic hypermutation of its heavy chain was the highest observed among VH3-53/66 mAbs, and its light chain was also quite hypermutated (**Figure 1C**). These striking genetic features demonstrated the uniqueness of 19-77 and prompted further studies.

To understand the molecular basis for the neutralization breadth and potency of 19-77, we then visualized its Fab fragment in complex with the D614G spike (**Figures 1D, S2A and S2B**) by single-particle cryo-electron microscopy (cryo-EM). The Fab was predominantly bound to the spike protein in a three-RBD-up conformation, like other VH3-53/66 class antibodies targeting the class 1 region[37]. The primary interaction between the 19-77 heavy chain and the RBD was mediated by CDRH1 and CDRH2, with hydrogen bonds to A475, N487, Y473, D420, and Y421 (**Figure 1E**). The CDRH3 region formed two hydrogen bonds with the RBD: one between R97 and the backbone carbonyl of N487, and another between E102 and Y489. On the other hand, the 19-77 light chain made contacts with the apical ridge of the RBD via its CDRL1 and CDRL3 (**Figure 1F**).

Structural explanation for the loss of 19-77 activity against certain Omicron subvariants

The antibody footprint of 19-77 on the RBD largely overlapped with the human ACE2 receptor binding site (**Figure 2A**). Sequence conservation analysis indicated that most regions of its epitope are relatively conserved, except for the upper half of the left shoulder, which exhibits significant sequence variations at positions 455, 456, 475, 478, and 486. These specific residues have undergone frequent mutations in certain recent subvariants, such as EG.5.1, HK.3, JF.1, and JD.1.1. It is therefore not surprising that the neutralizing activity of 19-77 against HK.3 (XBB.1.5 carrying Q52H and L455F/F456L mutations) and JF.1 (XBB.1.5 carrying E180V, L455F/F456L, and K478R) decreased by 14- and 42-fold, respectively, compared with that against XBB.1.5 (**Figure 1B**). The inactivity of 19-77 against JD.1.1 is likely due to its A475V mutation that causes a steric clash with CDRH1 (**Figure 2B**). To further understand the resistance mechanism of L455F/F456L mutations to the neutralization by 19-77, we determined the structure of 19-77 Fab in complex with the RBD of EG.5.1 by X-ray crystallography, as well as the cryo-EM structures of the D614G RBD and the HK.3 RBD

178 in complex with the Fabs of 19-77 and S309 (sotrovimab) (**Figure S2**), a non-overlapping mAb
179 used to increase the molecular mass for visualization by cryo-EM. Compared with the D614G
180 RBD (**Figure 2C**), the change from phenylalanine (F) to leucine (L) at residue 456 in the
181 EG.5.1 RBD reduced hydrophobic interactions with $P100_{HC}$ in the CDRH3 of 19-77 (**Figure**
182 **2D**). Additionally, the L455F mutation in HK.3 introduced a minor van der Waals clash with
183 $P100_{HC}$ (**Figure 2E**).
184
185 **Optimization of 19-77**
186
187 Given the minor to moderate steric clashes between the RBDs of resistant viruses and 19-77,
188 we explored the possibility of optimizing the antibody to accommodate for the resistance
189 mutations. Utilizing in-silico modeling and the energy-calculation algorithm FoldX[38], we
190 performed saturation mutagenesis on each residue of both the heavy and light chain, comparing
191 the binding energy changes (ΔΔG) between each mutant and the original 19-77 in complex
192 with the HK.3 RBD that contained the L455F/F456L mutations. Both beneficial and
193 detrimental mutations were identified (**Figure S3A**; data for light chain not shown).
194 Interestingly, substitutions at residue R71 in framework region 3 of the heavy chain
195 consistently predicted a moderately beneficial effect (~0.5 kcal/mol) on the binding of 19-77
196 to the HK.3 RBD. We then conducted alanine scanning on the antigen-contact residues of both
197 heavy and light chains of 19-77, in addition to the residue R71, followed by testing each
198 modified antibody for neutralization against JD.1.1, HK.3, EG.5, and EG.5-A475V (**Figures**
199 **3A, S3B and S3C**). Only the R71A mutation significantly enhanced the neutralization activity
200 of 19-77 against the viruses tested, including the restoration of neutralizing activity against
201 JD.1.1 and EG.5-A475V. We therefore introduced the other 18 possible amino-acid
202 substitutions to the R71 position of 19-77 and then evaluated their neutralization efficacy
203 against the same panel of resistant viruses (**Figure S3D**). Except for R71K, all other
204 substitutions resulted in not only improved neutralization activities against EG.5 and HK.3
205 relative to the original antibody, but also restoration of activity against JD.1.1 and EG.5-A475V.
206 Overall, the extent of improvement for these mutant antibodies (19-77Δs) ranged from 3-
207 to >100-fold, with aliphatic substitutions R71A, R71L, and R71V being the best (**Figures 3B**
208 **and S3D**).
209
210 Structural analysis showed that R71 of 19-77 forms hydrogen bonds with S30 of CDRH1 and
211 P53 of CDRH2, likely contributing to antibody stability (**Figure 3C**). Additional modeling
212 indicated that mutating R71 could disrupt these hydrogen bonds, with the exception of R71K,
213 which could also form similar interactions (**Figure 3D**). We then hypothesized that R71 might
214 restrict the motion of CDRH1 and CDRH2 of 19-77, and that mutating this arginine could lead
215 to greater antibody flexibility. To test this hypothesis, we conducted molecular dynamics (MD)
216 simulations for 19-77 with either arginine or alanine at position 71 of the heavy chain. The
217 results showed that A71 increased the range of motion of the heavy-chain CDRs compared to
218 R71 (**Movie 1**). Moreover, the fluctuations in the movement of each residue for the A71 variant
219 of 19-77 were noticeably greater than those in the original antibody, especially within the
220 CDRs (**Figure 3E**). These findings, in turn, suggested that the increased flexibility of the A71

221 variant could allow the antibody to better accommodate for certain mutations in the SARS-
222 CoV-2 spike.
223
224 We next assessed the in vitro neutralizing activity of the R71A, R71L, and R71V versions of
225 19-77 (designated 19-77ΔA, 19-77ΔL, and 19-77ΔV, respectively) against a large pseudovirus
226 panel comprising of 32 SARS-CoV-2 variants and 5 SARS-CoV-2-like sarbecoviruses.
227 Control antibodies included the original 19-77, along with the recently authorized pemivibart
228 (VYD222)[33] and a published broadly neutralizing mAb, P4J15[39] (**Figure 4**). The engineered
229 19-77 variants consistently showed better virus neutralizing potency and breadth compared to
230 the parental antibody. Importantly, against viruses that are widely circulating today, the
231 improvements were substantial: 7.7-to-9.2-fold for JN.1, 6.2-to-7.8-fold for KP.2, 8.1-to-13.3-
232 fold for KP.3, 16.2-to-21.6-fold for KP.3.1.1, and >50.0-to-147.1-fold for XEC, with the latter
233 two being most relevant presently. The activity P4J15 was either severely impaired or knocked
234 out by JN.1 and its progeny viruses. Pemivibart lost potency against recent JN.1 sublineages,
235 particularly KP.3.1.1 and XEC. These results showed that the optimized 19-77 mAbs possess
236 the requisite antiviral properties to be considered as candidates for clinical development,
237 pending a full developability assessment. Reassuringly, the three mutations at R71 did not
238 adversely impact antibody expression, aggregation propensity, or pharmacokinetics in mice
239 (**Figure S4**).
240
241 **Impact of R71 mutations on other VH3-53/66 class of mAbs to the viral spike**
242
243 Monoclonal 19-77 belonged to the VH3-53/66, multi-donor class of SARS-CoV-2 neutralizing
244 mAbs that target the class 1 region of RBD[37]. We therefore explored whether the same set of
245 R71 mutations could similarly benefit other members of this antibody class. Mutations R71A,
246 R71L, and R71V were then introduced into five VH3-53/66 class mAbs, including BD56-
247 1302[40], BD56-1854[40], Omi-3[41], 19-79 (our unpublished mAb), BD57-0129[40], and BD-515[42],
248 as well as two non-VH3-53/66 class mAbs, C68.59[29] and Omi42[41], serving as controls. The
249 original mAbs and their modified antibody variants were then assayed for their neutralizing
250 activity against a panel of pseudoviruses (**Figure S5**). All unmodified mAbs showed partial
251 or complete loss of neutralizing activity against some later Omicron subvariants such as EG.5.1,
252 HK.3, JD.1.1, and JN.1. In contrast, every modified VH3-53/66 mAb exhibited improved
253 neutralization capability, albeit with varying magnitudes (3- to >100-fold), whereas no
254 improvement was observed for non-VH3-53/66 mAbs (**Figures 5 and S5**). In fact, a number
255 of modified mAbs regained the ability to neutralize subvariants that had been completely
256 resistant to their unmodified counterparts. For example, BD57-0129 failed to neutralize JN.1
257 or HK.3, but its modified counterparts neutralized both viruses robustly. The extension of the
258 benefit of R71 mutations to mAbs other than 19-77 suggests that the responsible mechanism is
259 not likely to operate solely at the interface with the paratope. Instead, the broader benefit
260 observed is consistent with the hypothesis of greater conformational flexibility of the antibody
261 CDRs discussed previously. Additionally, antibodies using VH3-53 in the human B-cell
262 repertoire very rarely carry a mutation at R71 (**Figure S6**), highlighting the uniqueness of our
263 engineered mAbs compared to those found after SARS-CoV-2 infections.
264

265 **Molecular insights into enhanced virus neutralization by 19-77ΔV**
266
267 To further explore the mechanism of the enhancement of virus neutralization by mutating R71,
268 we determined two additional cryoEM structures: the Fabs of 19-77ΔV and S309 in complex
269 with HK.3 or JD.1.1 RBD at 2.9 Å and 3.1 Å resolution, respectively (**Figures 6A and S2**).
270 We then compared these structures by aligning their RBDs with that of the 19-77-D614G
271 complex and measuring the alpha carbon (Cα) distances for each heavy chain residue in 19-77
272 against the D614G complex. The analysis showed that the Cα distances in 19-77ΔV, when
273 bound to HK.3 and JD.1.1 RBDs, were significantly greater (0.99 Å and 0.91 Å, respectively)
274 compared to the original 19-77 in complex with HK.3 RBD (0.76 Å) (**Figure 6B**). Moreover,
275 the motion of the CDRH1 and CDRH2 were observed directly across these structures, and the
276 valine substitution at residue 71 resulted in the loss the hydrogen bonds that had existed
277 between R71 and the residues S30 and P53 in the heavy chain (**Figure 6C**). In addition, the
278 CDRH3 in 19-77ΔV exhibited a shift of 1 Å compared to the original 19-77, resulting in an
279 increased distance (from 3.3 Å to 3.6 Å) between residues P100 and F455 (**Figure 6D**). This
280 change mitigated the slight van der Waals clash between these two residues in HK.3 RBD and
281 19-77 complex (**Figure 2E**). Lastly, the distance between V475 in the JD.1.1 RBD and N32
282 of the heavy chain of 19-77ΔV increased to 3.2 Å from the 2.0 Å found in the original 19-77
283 bound to D614G RBD (**Figure 6E**), showing the mitigation of steric hindrance caused by the
284 A475V mutation. Collectively, these findings support the notion that 19-77Δ mAbs are indeed
285 more flexible and therefore more accommodating for the mutations found in emerging SARS-
286 CoV-2 variants.
287
288 **In vitro selection of SARS-CoV-2 resistant to 19-77ΔV**
289
290 Although the SARS-CoV-2-neutralization breadth and potency of the optimized 19-77 variants
291 were impressive (**Figure 4**), our expectation was that the virus will still find a way to escape
292 given its history of evading all COVID-19 mAbs authorized to date. We therefore undertook
293 two sets of in vitro studies to define its mutational pathways to resist 19-77ΔV. First, we
294 performed serial passaging of the authentic JN.1 virus in increasing antibody concentrations
295 (0.1 to 50 μg/mL) in Vero-ACE2-TMPRSS2 cell over 15 days (under 3 days per passage).
296 After five passages, a resistant virus was sequenced and found to carry mutations F456S and
297 K554E (**Figure 7A**). When these mutations were introduced into the JN.1 pseudovirus, the
298 resultant pseudovirus showed a 33-fold greater resistance to 19-77ΔV, and even more to 19-
299 77. Additional studies showed that the antibody evasion was attributable solely to F456S,
300 while K554E partially compensated for the loss in viral fitness (**Figures S7A and S7B**).
301 Notably, this combination of mutations is extremely rare (0.0002%) in the GISAID database.
302
303 Second, we also utilized a replication-competent VSV bearing the JN.1 spike to select for
304 variants that could escape from 19-77ΔV. This selection was performed in 66 replicates in 24-
305 well plates, involving four rounds of selection over 8 days in Vero-E6-TMPRSS2-T2A-ACEs
306 cells with increasing concentrations of 19-77ΔV (0.4 to 50 μg/mL). At the end of this process,
307 escape variants were detected in in 11 wells, and sequencing of their spike genes revealed 8

distinct single or double mutations (**Figure 7B**). Notably, all these mutations were rarely found in the GISAID database, with frequencies ranging from 0% to 0.01%, and each of the pseudoviruses constructed with these mutations exhibited impaired infectivity compared to the JN.1 pseudovirus, ranging from 1% to 33% (**Figures 7B and S7C**). Furthermore, these pseudoviruses demonstrated increased resistance to soluble hACE2 inhibition (**Figure 7B and S7D**), indicating a loss in receptor affinity, perhaps accounting in part for their reduced infectivity. Single mutations G485D and Y489H, both residing in the RBD, decreased the neutralization activity of 19-77ΔA/L/V considerably (9- to 121-fold), whereas the remaining mutations completely abolished the neutralization activity of the three optimized mAbs (**Figures 7B and S7D**).

In silico structural analysis showed that each of the escape viruses contained a mutation within the epitope of 19-77ΔV that impaired antibody binding (**Figure 7C**). A475D, G476D, and N487H caused steric hindrance to antibody binding, F465S mutation and residue S455 in JN.1 significantly reduced hydrophobic interactions between the antibody and RBD. Furthermore, both Y473S and Y489H abolished hydrogen bonds with the antibody, contributing to the dramatic drop in neutralization observed for the escape viruses with these mutations.

DISCUSSION

In this study, we present findings on the characterization of a human IGHV3-53-derived monoclonal antibody, 19-77, which exhibited neutralizing activity against most but not all SARS-CoV-2 variants (**Figures 1B and 4**). Strikingly, 19-77 featured the shortest CDRH3 (9 amino acids) while containing the highest degree of somatic hypermutations among its class of mAbs (**Figure 1C**). Structural analysis revealed that 19-77 recognized the spike RBD in the "up" position (**Figure 1D**), and its epitope overlapped with the ACE2 footprint (**Figure 2A**). Subsequent in silico energy calculations (**Figure S3A)** and empirical mutagenesis experiments (**Figures 3A and 3B**) yielded modified antibodies 19-77ΔA, 19-77ΔL, and 19-77ΔV, each of which neutralized all 32 SARS-CoV-2 variants tested, including KP.3.1.1 and XEC that are so prevalent today (**Figure 4**). These optimized antibodies joined a limited list of human mAbs that possess sufficiently potent neutralizing activity against all viral variants, such as SA55[43], BD55-1205[44], and VIR-7229[45] that target an epitope overlapping with that of 19-77, as well as CYFN1006-1[46] that targets a RBD class 3 epitope. However, we showed that SARS-CoV-2 could easily escape from neutralization by 19-77ΔV in vitro (**Figure 7**). In fact, the virus found multiple solutions to evade our optimized antibody, albeit with a fitness cost. Such an outcome was, more or less, expected given how SARS-CoV-2 has evolved in the population to render inactive all clinical mAbs authorized prior to 2024. Indeed, pemivibart (VYD222) that was authorized only months ago for use as prophylaxis against COVID-19 in immune deficient subjects is already seriously threatened by the emergence of KP.3.1.1 and XEC subvariants[35,47,48].

351 It has been a daunting challenge, as well as a frustrating endeavor, to develop therapeutic or
352 prophylactic mAbs to keep up with the rapid pace of SARS-CoV-2 evolution. Yet the reality
353 is that millions of individuals worldwide are sufficiently immunocompromised that they cannot
354 benefit from the protection conferred by COVID-19 vaccines. Such persons need effective
355 prophylaxis with passively administered virus-neutralizing mAbs, as was conferred previously
356 by the combination of tixagevimab and cilgavimab known as Evusheld[49] and presently by
357 pemivibart[33]. Going forward, we believe one of our optimized 19-77Δ mAbs would qualify as
358 a compelling candidate for clinical development given its superior potency and breadth against
359 all SARS-CoV-2 variants known to date (**Figure 4**), as well as its lack of discernible
360 developability challenges to date (**Figure S4**). The potential clinical utility of an optimized
361 19-77Δ could be further improved if used in combination with a non-competing, broadly
362 neutralizing mAb like CYFN1006-1[46].
363
364 Herein, we also present a unique strategy for optimizing the activity of a monoclonal antibody
365 by increasing its conformational flexibility. Traditionally, antibody engineering had been
366 focused primarily on increasing the binding affinity using a number of approaches, including
367 chain shuffling[50,51], site-directed mutagenesis[52], phage and other display technologies[53-57], and
368 structure-based or artificial-intelligence-guided methods[58-60]. Such methodologies, typically,
369 had been designed to increase antibody affinity by modifying the CDR residues at the antibody-
370 antigen interface. Other antibody approaches to optimize antibody activity included the use of
371 multivalency with the creation of "multabodies"[61], or the strategic addition of a glycan to bulk
372 up a steric hindrance effect[62]. The framework regions of a mAb were seldom touched, because
373 they are crucial for maintaining the proper orientation and conformation of the CDRs[63,64]. In
374 our study on 19-77, however, in silico energy calculations indicated that a single amino-acid
375 substitution at residue 71 in framework region 3 of the heavy chain could improve antibody
376 binding to the viral spike (**Figure S3A**), which was proven correct experimentally by replacing
377 the arginine with any other natural amino acid except for lysine (**Figures 3A, 3B, and 4**). The
378 improved activity of optimized 19-77Δ mAbs was attributable to the loss of hydrogen bonding
379 by R71 (**Figures 3C and 6C**), leading to greater flexibility of the CDRs as shown by molecular
380 dynamics (**Figure 3E**) and structural analyses (**Figure 6**). This enhanced conformation
381 flexibility, in turn, allowed each optimized antibody to be more tolerant of mutations within or
382 near its epitope, ultimately resulting in the striking SARS-CoV-2 neutralization potency and
383 breadth observed (**Figure 4**). Remarkably, this optimization strategy was also successfully
384 applied to 6 other IGHV3-53/3-66-derived human mAbs that target the same epitope cluster as
385 19-77 (**Figure 5**). But its applicability did not extend to other SARS-CoV-2-neutralizing mAbs
386 that utilize other VH germline genes, suggesting a specific mutation at framework residue 71
387 is not likely to confer a generalizable benefit to other mAbs. Nevertheless, the general concept
388 of modifying antibody conformational flexibility should be further explored in other settings
389 by other means. Increasing conformational rigidity could lead to improved antibody-antigen
390 affinity, as has been reported for an IGHV4-59-encoded anti-lysozyme mAb[65]. On the other
391 hand, increasing conformational flexibility, as shown in this study, could allow the antibody to
392 better tolerate sequence variations in the target antigen. Such an approach may be useful for
393 monoclonal antibodies directed to polymorphic antigens or surface proteins of rapidly evolving

394 viruses such as HIV-1, coronaviruses, influenza viruses, and hepatitis C virus. It may be
395 another important conceptual tool in our antibody engineering armamentarium.

FIGURES and LEGENDS

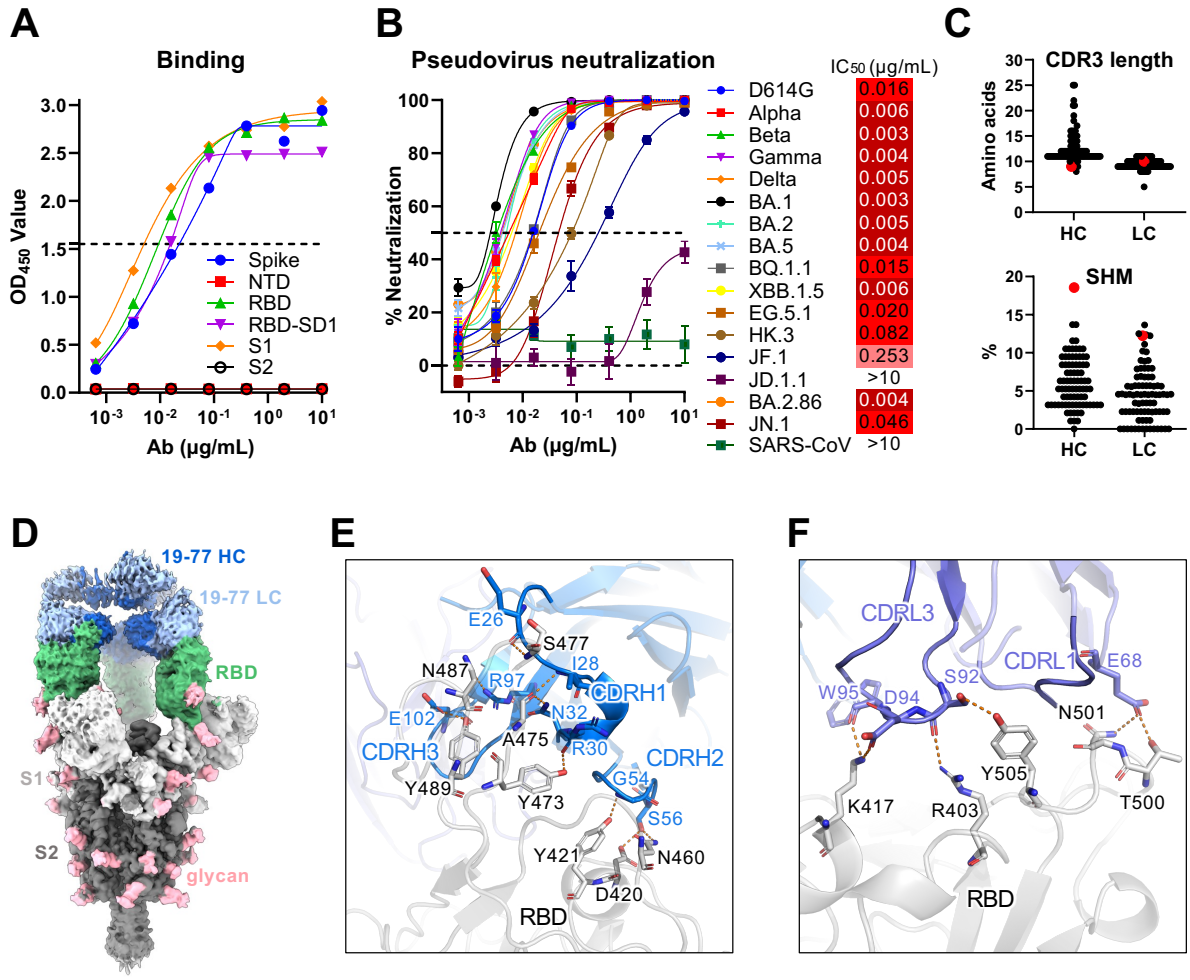

Figure 1. Neutralization activity and epitope mapping of 19-77.

A. Binding of 19-77 to the indicated antigens of SARS-CoV-2 D614G tested by ELISA.

B. Neutralization IC_{50} values of 19-77 against pseudotyped SARS-CoV-2 variants and SARS-CoV, with the IC_{50} of each virus is denoted. Neutralization curves are shown as mean ± standard error of mean (SEM).

C. Complementarity-determining region 3 (CDR3) lengths and somatic hypermutations (SHM) of 19-77 heavy chain (HC) and light chain (LC), compared with other 3-53 and 3-66 antibodies. 19-77 is highlighted in red.

D. Cryo-EM reconstruction of 19-77 in complex with the SARS-CoV-2 D164G spike protein, at a resolution of 2.45Å.

E. Key interactions between 19-77 heavy chain and the D614G RBD. Hydrogen bonds are shown as the orange dashed lines.

F. Key interactions between 19-77 light chain and the D614G RBD. Orange dashed lines indicate hydrogen bonds.

See also **Figure S1 and S2**.

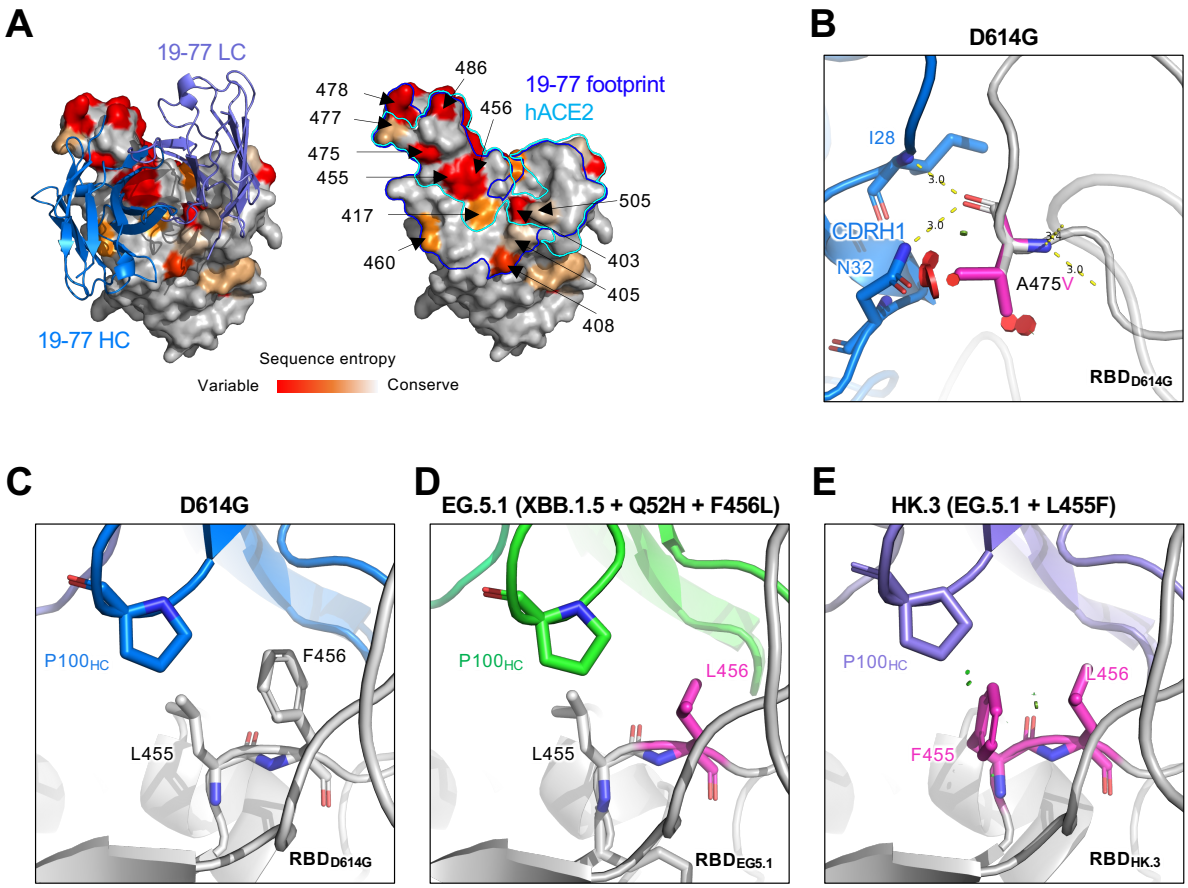

Figure 2. Sequence conservation and resistant mutations in the 19-77 epitope.

A. Top view of the RBD inner face in complex with the 19-77 antibody. 19-77 heavy chain and light chain are shown in marine and light blue, respectively. The residues in the RBD are colored by the sequence entropy in circulating SARS-CoV-2 variants. The blue and cyan boundaries show the footprints of 19-77 and human ACE2 (hACE2), respectively.

B. Structure modeling of how A475V on the RBD affects 19-77 neutralization. The clashes are shown as red plates.

C-E. Comparison of residues 455 and 456 on RBD and P100$_{HC}$ in D614G (**C**), EG.5.1 (**D**) and HK.3 (**E**) structures. The van der Waals clashes are shown as green plates.

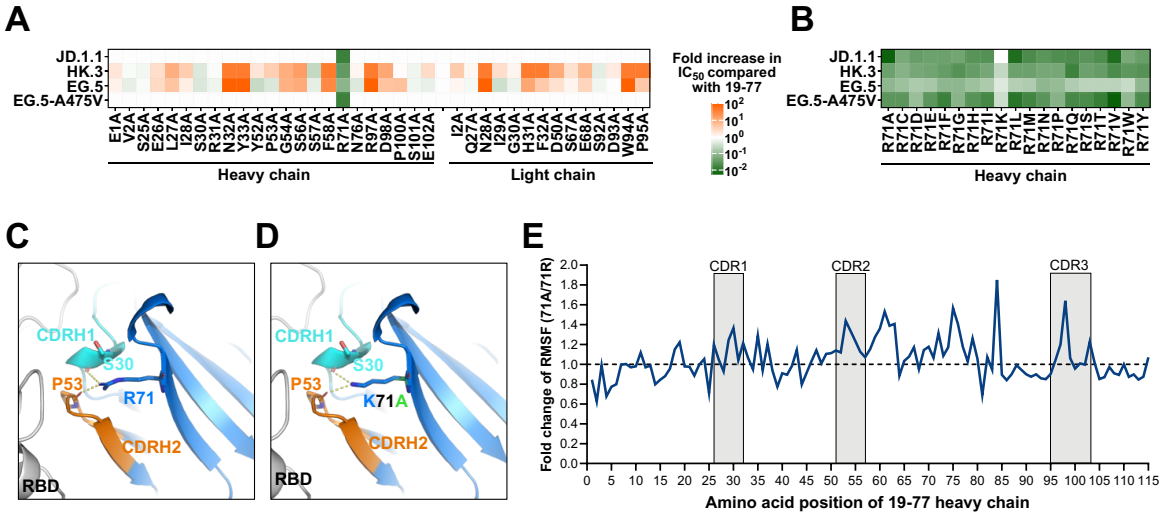

Figure 3. Optimization of 19-77 in neutralization activity.

A. Neutralization of 19-77 carrying individual mutations on both heavy and light chains, in comparison with the wildtype 19-77 antibody.

B. Neutralization of 19-77 carrying various amino acid substitutions at R71 on the heavy chain, compared with the wildtype 19-77 antibody.

C. Depiction of the interactions between R71 and the heavy chain CDRs H1 (cyan) and H2 (orange) in 19-77. Dashed lines indicate the presence of hydrogen bonds.

D. Structure modeling of K71 (blue) and A71 (green) with HCDRs of 19-77. Dashed lines indicate the presence of hydrogen bonds between 19-77ΔK.

E. Comparison of the RMSF between the Fab regions of 19-77 and its mutant 19-77ΔA. The Y-axis represents the fold change in RMSF per residue in 19-77ΔA relative to 19-77. The X-axis displays the positional numbering of residues within the antibody. RMSF, per-residue root-mean-square fluctuation.

See also **Figure S3**.

Clade	Pseudovirus	19-77	19-77 mutants			Control Abs	
			R71A	R71L	R71V	P4J15	VYD222
SARS-CoV-2 variants	D614G	0.015	0.009	0.007	0.009	0.004	0.013
	B.1.1.7 (Alpha)	0.003	0.003	0.003	0.003	0.003	0.012
	B.1.351 (Beta)	0.003	0.003	0.002	0.002	0.003	0.017
	P.1 (Gamma)	0.002	0.002	0.002	0.002	0.003	0.028
	B.1.617.2 (Delta)	0.005	0.004	0.004	0.004	0.003	0.011
	BA.1	0.001	0.001	0.001	0.001	0.001	0.203
	BA.2	0.008	0.004	0.004	0.004	0.003	0.102
	BA.5	0.006	0.004	0.004	0.004	0.010	0.101
	BA.2.75	0.015	0.007	0.007	0.009	0.004	0.516
	CH.1.1	0.010	0.006	0.009	0.009	0.026	0.381
	DV.7.1	0.285	0.019	0.031	0.025	1.179	1.250
	XBC.1.6	0.007	0.003	0.005	0.004	0.033	0.183
	BQ.1.1	0.011	0.008	0.006	0.009	0.023	0.260
	XBB.1.5	0.008	0.005	0.004	0.008	0.059	0.215
	XBB.1.16.6	0.054	0.004	0.002	0.003	0.017	0.243
	XBB.2.3	0.012	0.007	0.008	0.009	0.018	0.263
	EG.5.1	0.020	0.008	0.006	0.008	0.039	0.233
	FL.1.5.1	0.056	0.006	0.006	0.008	0.039	0.240
	JF.1	0.156	0.008	0.006	0.008	0.227	0.343
	HV.1	0.052	0.006	0.005	0.006	0.020	0.159
	HK.3	0.107	0.007	0.006	0.008	1.340	0.304
	JD.1.1	>10	0.033	0.032	0.058	0.355	0.288
	BA.2.87.1	0.026	0.008	0.009	0.009	0.003	1.043
	BA.2.86	0.006	0.003	0.003	0.003	0.081	0.459
	JN.1	0.046	0.005	0.005	0.006	>10	0.070
	JN.4	0.017	0.004	0.003	0.003	0.270	0.512
	LB.1	0.087	0.008	0.009	0.008	2.303	0.208
	KP.2	0.031	0.004	0.005	0.004	>10	0.148
	KP.3	0.585	0.044	0.072	0.068	0.729	0.554
	KP.2.3	0.107	0.015	0.009	0.005	>10	0.459
	KP.3.1.1	1.426	0.066	0.088	0.075	2.862	1.217
	XEC	>10	0.092	0.200	0.068	>10	1.998
SARS-CoV-2 like sarbecoviruses	GX-pangolin	1.878	0.302	0.317	0.163	>10	0.008
	RaTG13	0.005	0.003	0.002	0.003	0.004	>10
	BANAL52	0.027	0.015	0.007	0.011	0.007	0.008
	BANAL236	0.012	0.007	0.005	0.011	0.003	0.005
	GD-pangolin	0.009	0.006	0.004	0.006	0.003	0.003

IC_{50} (μg/mL) <0.01 | 0.01-0.1 | 0.1-1 | 1-10 | >10

Figure 4. Neutralization activity of 19-77 and 19-77ΔA/L/V against the indicated pseudoviruses. Neutralization IC_{50} values of the indicated antibodies against a panel of pseudotyped viruses, including SARS-CoV-2 variants and SARS-CoV-2-like sarbecoviruses. See also **Figure S4**.

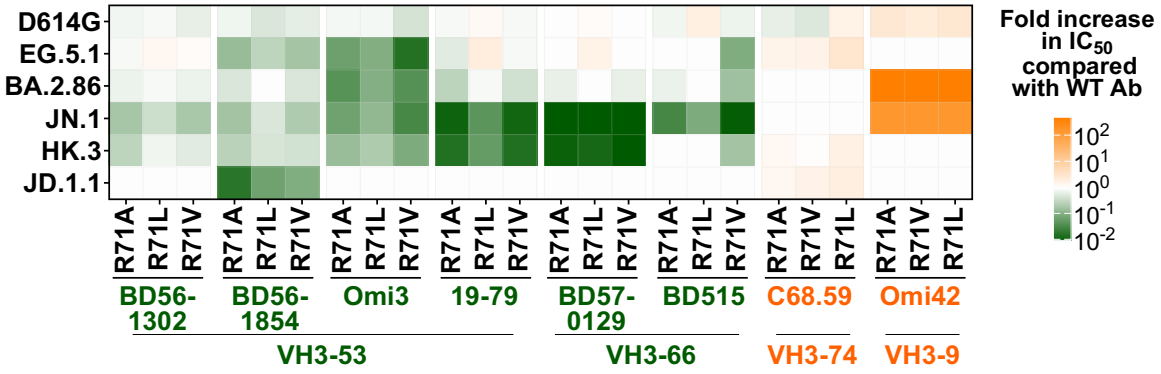

Figure 5. R71A/L/V sensitize the neutralization activity of other VH3-53/66 class antibodies. Neutralization of the indicated antibodies from VH3-55/66 and other classes carrying R71A/L/V mutations, compared with the respective wildtype (WT) antibodies. See also **Figure S5 and S6**.

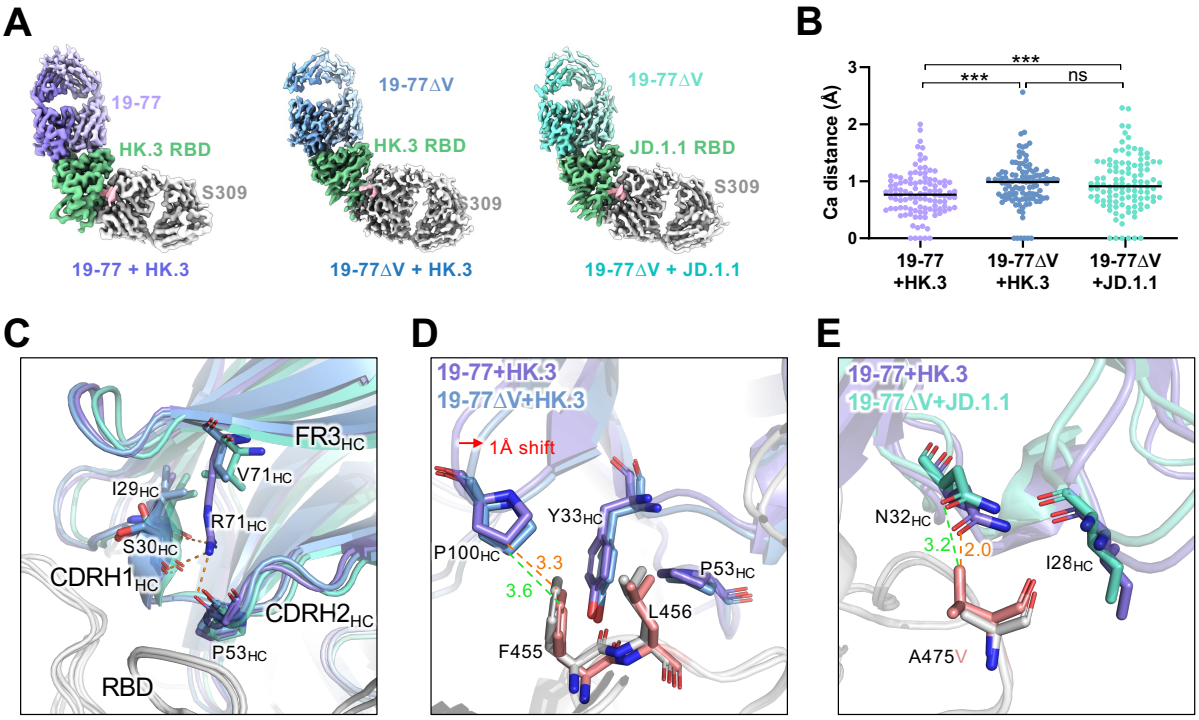

Figure 6. Molecular basis of 19-77ΔV accommodating mutations in HK.3 and JD.1.1.

A. Cryo-EM maps of 19-77 and 19-77ΔV Fabs bound to SARS-CoV-2 RBD variants.

B. Distribution of Cα distance for the heavy chain residues of 19-77 in **A** compared with 19-77 in the D614G complex. The structures are aligned based on RBD.

C. Comparison of CDRH1, CDRH2, and R71V in the alignments of 19-77 structures. The hydrogen bonds are shown as orange dashed lines.

D. Interaction details of $P100_{HC}$ in 19-77 and 19-77ΔV with F455 and L456 in the HK.3 RBD. The orange and green dashed lines represent the distances between $P100_{HC}$ and F455 in 19-77 and 19-77ΔV, respectively.

E. Interaction details of $N32_{HC}$ in 19-77 and 19-77ΔV with A475V in the D614G and JD.1.1 RBDs. The orange and green dashed lines represent the distances between V475 and N32 in 19-77 and 19-77ΔV, respectively.

See also **Figure S2**.

A

mAb	Authentic virus for escape selection	Selection passages	Escape mutations	Frequency of mutations in GISAID	Relative infectivity of pseudotyped escape variant	Fold change in IC_{50} of pseudotyped escape variants compared with the relative WT virus		
						19-77	19-77ΔV	hACE2
19-77ΔV	JN.1	P5	F456S+K554E	0.0002%	64%	<-99	-33	-2.2

B

Escape mutations under sequentially increased 19-77ΔV concentrations				Properties of escape variants from 50 μg/ml of 19-77ΔV selection					
				Frequency in GISAID	Relative infectivity	Fold change in IC_{50} compared with JN.1			
No.	4 μg/ml	20 μg/ml	50 μg/ml			19-77ΔA	19-77ΔL	19-77ΔV	hACE2
1	T393A	T393A/Y489H	T393A/Y489H	0%	1%	<-1214	<-1097	<-1236	<-114
2	F456S	F456S	F456S/E471G	0%	2%	<-1214	<-1097	<-1236	-103
3	Y473S	Y473S	Y473S	0.00036%	1%	<-1214	<-1097	<-1236	<-114
4	A475D	A475D	A475D	0.0035%	2%	<-1214	<-1097	<-1236	<-114
5	G476D	G476D	G476D/N487H	0%	1%	<-1214	<-1097	<-1236	<-114
6	G485D	G485D	G485D	0.010%	33%	-9.0	-12	-10	-12
7	Y489H	Y489H	Y489H	0.0028%	18%	-44	-57	-121	-27
8	Y489H	Y489H	N405D/Y489H	0%	22%	<-1214	<-1097	<-1236	-34

Resistant	<-1000	<-100	<-10	<-3

C

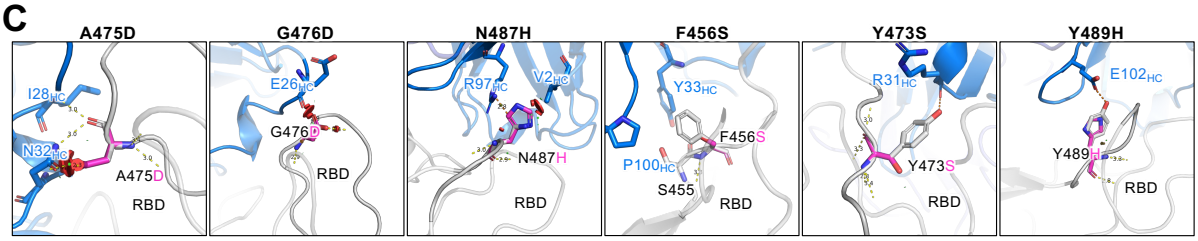

Figure 7. In vitro selection of 19-77 resistant mutations.

A. Properties of the authentic JN.1 escape variant selected under the pressure of 19-77ΔV.

B. Properties of the replication-competent VSV-JN.1 escape variants selected under the pressure of 19-77ΔV.

C. Structural modeling of how A475D, G476D, N487H, F456S, Y473S, and Y489H affect 19-77 neutralization. The clashes are shown as red plates, and the hydrogen bonds are shown as orange dashed lines.

See also **Figure S7**.

SUPPLEMENTAL INFORMATION

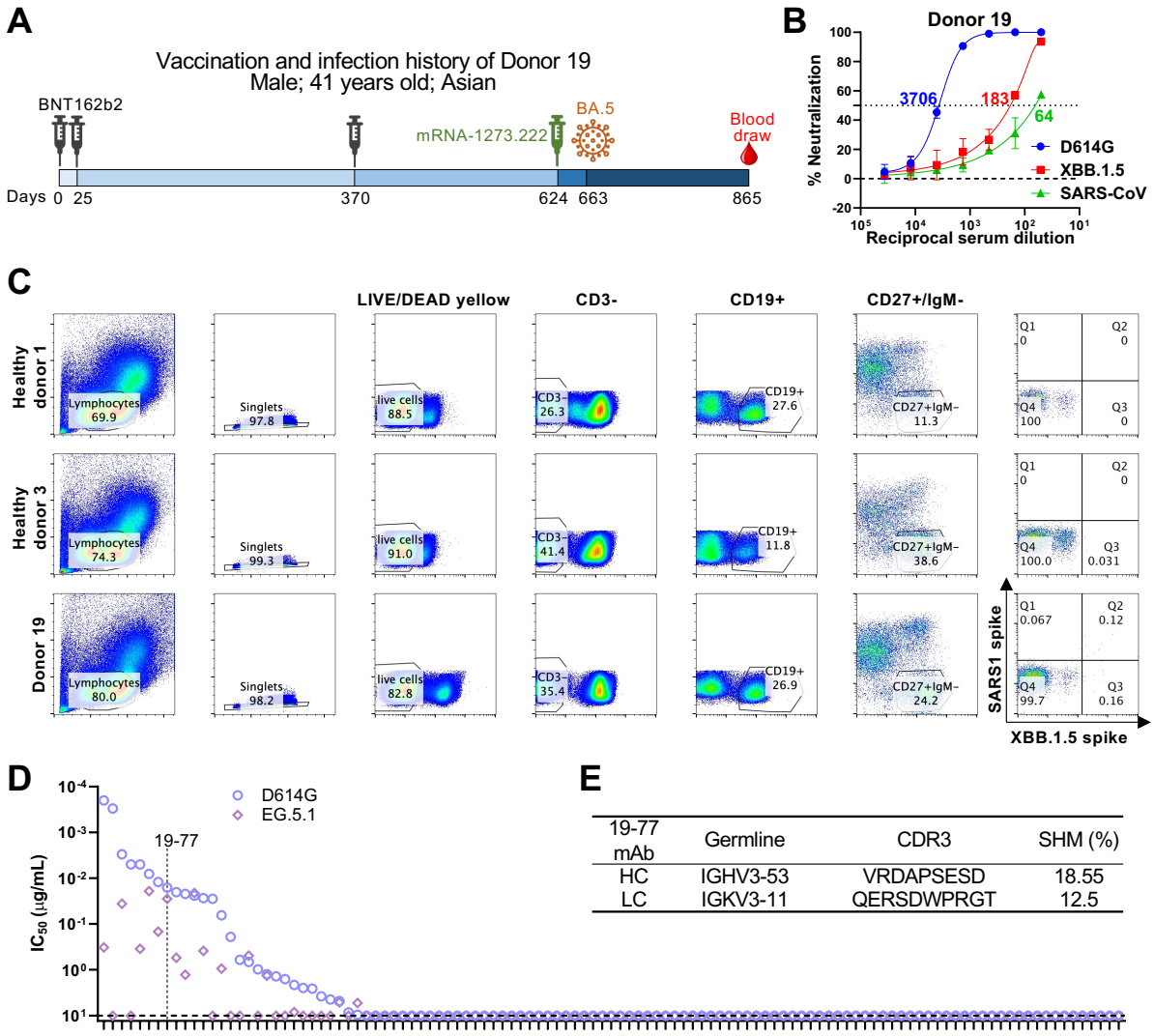

19-77 mAb	Germline	CDR3	SHM (%)
HC	IGHV3-53	VRDAPSESD	18.55
LC	IGKV3-11	QERSDWPRGT	12.5

Figure S1. Clinical information and sorting strategy.

A. Clinical information of donor 19, whose blood sample was collected for neutralizing antibody evaluation and B cell sorting.

B. Neutralization activity of serum from donor 19 against D614G, XBB.1.5, and SARS-CoV. Neutralization ID_{50} titer against each virus is denoted. Data are shown as mean ± SEM (standard error of the mean).

C. Sorting strategy used to isolate XBB.1.5 spike and/or SARS-CoV spike specific B cells. B cells from Q2 and Q3 were collected and applied for downstream 10X Genomics analysis. Numbers in gates represent cell percentages.

D. Neutralizing IC_{50} values of the antibodies from donor 19 against D614G and EG.5.1. 19-77 is highlighted with a dotted line.

E. Germline genes, CDR3 amino acid sequences, and SHM percentages of 19-77 heavy and light chains.

See also **Figure 1**.

A

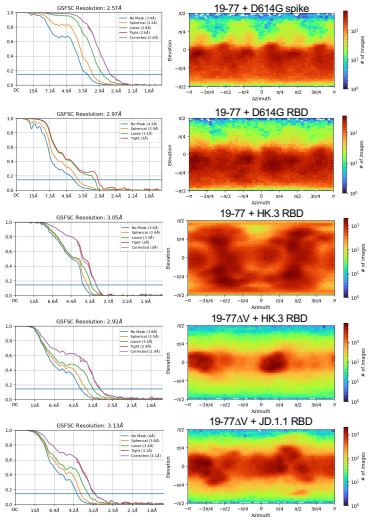

B

Cryo-EM data collection, refinement, and validation statistics for 19-77 samples

Antibody	19-77	19-77	19-77	19-77ΔV	19-77ΔV
Antigen	D614G spike	D614G RBD	HK.3 RBD	HK.3 RBD	JD.1.1 RBD
EMBD	EMD-45548	EMD-45543	EMD-45544	EMD-45545	EMD-45546
PDB		9CFE	9CFE	9CFG	9CFH
Data collection and processing					
Magnification	105,000	105,000	105,000	105,000	105,000
Voltage (kV)	300	300	300	300	300
Electron exposure (e–/Å^2)	58.06	58.06	58.06	58.06	58.06
Defocus rang (μm)	-0.8 to -2.0	-0.8 to -2.0	-0.8 to -2.0	-0.8 to -2.0	-0.8 to -2.0
Pixel size (Å/pix)	0.83	0.83	0.83	0.83	0.83
Symmetry impose	C1	C1	C1	C1	C1
Final particle images (no.)	329,845	329,845	2,155,249	1,931,787	1,025,102
Map resolution	2.8Å	3.1Å	3.3Å	3.2Å	3.4Å
FSC threshold (loose mask)	0.143	0.143	0.143	0.143	0.143
Refinement					
Model composition					
Non-hydrogen atoms		6382	6400	6402	6394
Protein residues		416	417	417	417
Ligands					
R.m.s. deviations					
Bond lengths (Å)		0.013 (2)	0.004 (0)	0.004 (0)	0.004 (0)
Bond angles (°)		1.928 (31)	0.625 (3)	0.744 (0)	0.747 (3)
Validation					
MolProbity score		1.32	1.74	1.47	1.25
Clashscore		0.31	4.68	5.63	2.50
Poor rotamers (%)		1.98	1.69	0.28	0.00
Ramachandran plot					
Favored (%)		92.20	95.38	97.08	96.59
Allowed (%)		6.83	4.38	2.92	3.16
Disallowed (%)		0.98	0.24	0.0	0.24
B factors (Å)					
Protein		41.52	65.72	147.56	58.15

C

X-ray diffraction data collection and refinement statistics

Antibody	19-77 Fab	19-77 Fab
Antigen	D614G RBD	EG.5.1 RBD
PDB ID	9CAW	9CAV
Data Collection		
Space group	$P2_1$	$P2_1$
Cell constants	94.9 115.5 108.2 90 110.68 90	94.9 116.2 109.2 90 110.4 90
Resolution range (Å)	34.43 - 2.916 (2.99 - 2.92)*	35.2 - 3.2 (3.1- 3.0)*
Total reflections	1561719 (1674)	86848 (514)
Unique reflections	237828 (1188)	43474 (1270)
Completeness (%)	99.28 (98.96)	97.74 (94.91)
Redundancy	6.6 (1.4)	2.0 (2.0)
I/σ	3.44 (0.89)	3.22 (1.29)
R-merge	5.1 (0.84)	0.085 (0.67)
CC1/2	1.0 (0.35)	0.69 (0.40)
Refinement		
Resolution range (Å)	34.3-2.91	34.5 - 3.2
Number of complexes per asymmetric unit	2	2
Rwork/Rfree	0.256/0.303	0.25/0.29
Number of atoms		
Protein	9342	8940
Ligands	0	0
Water	0	0
B-factors (Å^2)		
Protein	29.36	36.0
Ligands	-	-
Water	-	-
R.M.S deviations		
Bond lengths (Å)	0.011	0.012
Bond angles (°)	1.50	1.64
Ramachandran statistics		
Favored (%)	96.06	93.85
Allowed (%)	3.94	6.15
Outliers (%)	0	0

Figure S2. Cryo-EM and X-ray data for mAbs 19-77 and 19-77ΔV in complex with SARS-CoV-2 spike trimers or RBDs.

A. Global refinement Fourier Shell Correction curves showing the overall resolution of the indicated complexes.

B. Cryo-EM data collection and model refinement of the indicated complexes.

C. X-ray diffraction data collection and refinement statistics.

See also **Figure 1 and 6**.

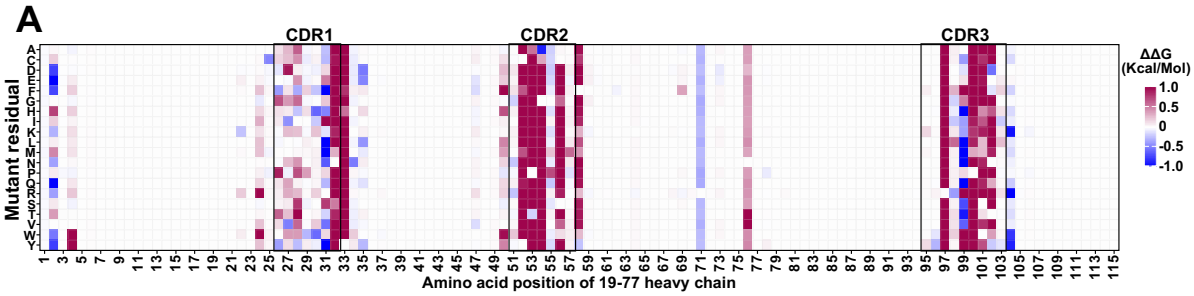

B

	IC50 (μg/mL)	JD.1.1	HK.3	EG.5	EG.5-A475V
	19-77	>10	0.229	0.098	>10
19-77 HC	E1A	>10	0.450	0.137	>10
	V2A	>10	0.202	0.060	>10
	S25A	>10	0.178	0.088	>10
	E26A	>10	0.570	0.281	>10
	L27A	>10	2.309	0.523	>10
	I28A	>10	0.940	0.156	>10
	S30A	>10	0.114	0.046	>10
	R31A	>10	0.210	0.069	>10
	N32A	>10	>10	>10	>10
	Y33A	>10	>10	>10	>10
	Y52A	>10	0.463	0.030	>10
	P53A	>10	0.887	0.046	>10
	G54A	>10	2.377	0.923	>10
	S56A	>10	3.750	1.092	>10
	S57A	>10	0.068	0.059	>10
	F58A	>10	>10	2.935	>10
	R71A	0.169	0.009	0.009	0.176
	N76A	>10	0.286	0.049	>10
	R97A	>10	>10	>10	>10
	D98A	>10	2.840	0.550	>10
	P100A	>10	0.241	0.584	>10
	S101A	>10	0.168	0.071	>10
	E102A	>10	0.619	0.062	>10

C

	IC50 (μg/mL)	JD.1.1	HK.3	EG.5	EG.5-A475V
	19-77	>10	0.229	0.098	>10
19-77 LC	I2A	>10	0.994	0.121	>10
	Q27A	>10	0.280	0.081	>10
	N28A	>10	>10	>10	>10
	I29A	>10	0.578	0.036	>10
	G30A	>10	0.294	0.066	>10
	H31A	>10	>10	1.244	>10
	F32A	>10	>10	0.440	>10
	D50A	>10	2.456	0.225	>10
	S67A	>10	0.528	0.127	>10
	E68A	>10	1.724	0.315	>10
	S92A	>10	0.135	0.074	>10
	D93A	>10	0.388	0.098	>10
	W94A	>10	>10	>10	>10
	P95A	>10	>10	0.469	>10

D

IC50 (μg/mL)	JD.1.1	HK.3	EG.5	EG.5-A475V
19-77	>10	0.170	0.062	>10
R71A	0.065	0.008	0.006	0.337
R71C	0.606	0.014	0.008	0.336
R71D	0.420	0.010	0.011	1.211
R71E	0.472	0.009	0.010	0.333
R71F	0.469	0.007	0.006	0.168
R71G	0.546	0.005	0.006	0.850
R71H	0.310	0.007	0.008	0.301
R71I	0.285	0.010	0.011	0.206
R71K	>10	0.048	0.030	3.394
R71L	0.095	0.008	0.013	0.115
R71M	0.241	0.008	0.012	0.195
R71N	0.324	0.010	0.006	0.321
R71P	0.259	0.010	0.007	0.82
R71Q	0.245	0.003	0.012	0.214
R71S	0.319	0.008	0.015	0.237
R71T	0.251	0.007	0.015	0.155
R71V	0.095	0.004	0.015	0.06
R71W	0.615	0.006	0.019	1.054
R71Y	0.434	0.005	0.006	0.234

<0.01	0.01-0.1	0.1-1	1-10	>10

Figure S3. Neutralizing IC_{50} values of 19-77 mutants.

A. Free energy change (ΔΔG) for saturation mutagenesis of the 19-77 heavy chain. Blue represents beneficial mutations, while red indicates mutations with adverse effects.

B. Neutralization IC_{50} values of 19-77 carrying the indicated mutations in the heavy chain.

C. Neutralization IC_{50} values of 19-77 carrying the indicated mutations in the light chain.

D. Neutralization IC_{50} values of 19-77 carrying various amino acid substitutions at R71 in the heavy chain.

See also **Figure 3**.

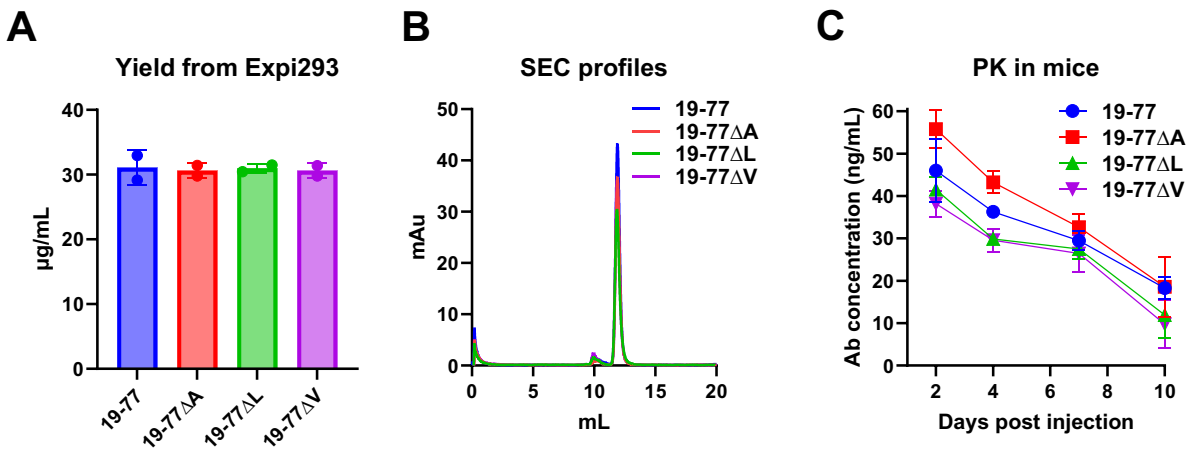

Figure S4. Biological properties of 19-77.

A. Yields of 19-77 and 19-77ΔA/L/V from transiently transfected Expi293 cells at day 4 post-transfection.

B. Size exclusion chromatography (SEC) profiles of 19-77 and 19-77ΔA/L/V antibodies.

C. Pharmacokinetics of 19-77 and 19-77ΔA/L/V in mice over 10 days after intraperitoneal injection. Data are shown as mean ± SEM (standard error of the mean).

See also **Figure 4**.

	Abs			Ab IC_{50} (ug/mL)					
				D614G	EG.5.1	BA.2.86	JN.1	HK.3	JD.1.1
VH3-53	BD56-1302	RBD class 1	WT	0.014	0.014	0.007	0.186	0.202	>10
			R71A	0.011	0.012	0.005	0.036	0.060	>10
			R71L	0.012	0.019	0.006	0.073	0.152	>10
			R71V	0.009	0.016	0.005	0.038	0.115	>10
	BD56-1854	RBD class 1	WT	0.008	0.027	0.002	0.022	0.111	10
			R71A	0.006	0.004	0.001	0.004	0.031	0.189
			R71L	0.004	0.008	0.002	0.011	0.053	0.697
			R71V	0.005	0.005	0.001	0.005	0.048	0.977
	Omi3	RBD class 1	WT	0.011	>10	0.467	>10	>10	>10
			R71A	0.009	0.668	0.021	0.685	1.505	>10
			R71L	0.009	0.991	0.048	1.324	2.232	>10
			R71V	0.005	0.172	0.020	0.331	0.912	>10
	19-79	RBD class 1	WT	0.013	0.073	0.007	>10	>10	>10
			R71A	0.011	0.042	0.002	0.116	0.165	>10
			R71L	0.016	0.160	0.006	0.484	0.582	>10
			R71V	0.011	0.062	0.003	0.124	0.162	>10
VH3-66	BD57-0129	RBD class 1	WT	0.013	0.003	0.003	>10	>10	>10
			R71A	0.013	0.003	0.002	0.028	0.107	>10
			R71L	0.015	0.005	0.003	0.064	0.132	>10
			R71V	0.013	0.003	0.002	0.035	0.090	>10
	BD515	RBD class 1	WT	0.022	>10	0.166	>10	>10	>10
			R71A	0.017	>10	0.115	0.322	>10	>10
			R71L	0.043	>10	0.157	0.913	>10	>10
			R71V	0.016	0.955	0.028	0.098	1.818	>10
VH3-74	C68.59	SD1	WT	0.048	0.108	>10	>10	0.081	0.073
			R71A	0.021	0.173	>10	>10	0.105	0.099
			R71V	0.025	0.179	>10	>10	0.085	0.120
			R71L	0.083	0.341	>10	>10	0.149	0.150
VH3-9	Omi42	RBD class 1	WT	0.020	>10	0.021	0.066	>10	>10
			R71A	0.056	>10	>10	>10	>10	>10
			R71V	0.048	>10	>10	>10	>10	>10
			R71L	0.057	>10	>10	>10	>10	>10

<0.01	0.01-0.1	0.1-1	1-10	>10

Figure S5. R71/A/L/V mutations rescue the neutralizing activities of VH3-53 and VH3-66 antibodies against SARS-CoV-2 escaping variants. The figure shows neutralization IC_{50} values of the indicated antibodies and their R71A/L/V mutants.
See also **Figure 5**.

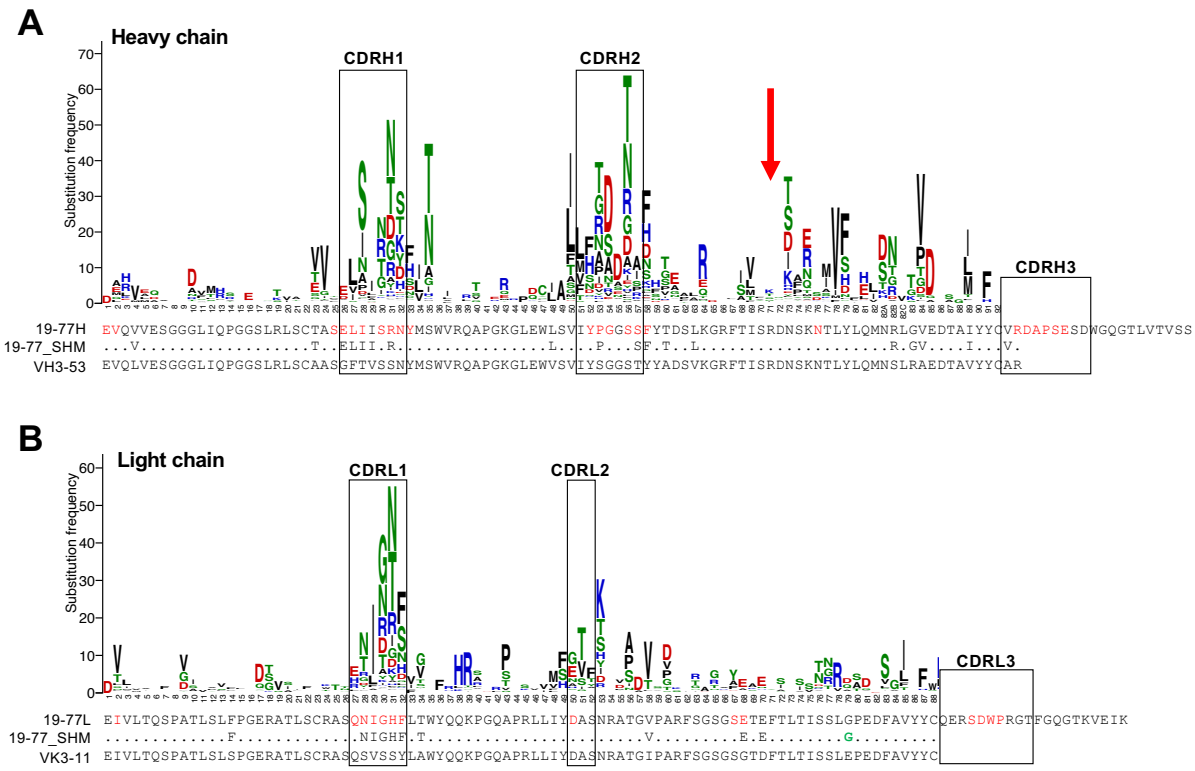

Figure S6. Gene-specific substitution profile for mAb 19-77.

A. The gene-specific substitution profiles (GSSP) for IGHV3-53 and the SHMs of 19-77 heavy chain. The red residues indicate the paratope residues of 19-77 heavy chain. R71 is highlighted by a red arrow.

B. GSSP for IGKV3-11 and the SHMs of 19-77 heavy chain. The red residues indicate the paratope residues of 19-77 light chain. The green residue indicates a rare mutation in 19-77 light chain.

See also **Figure 5**.

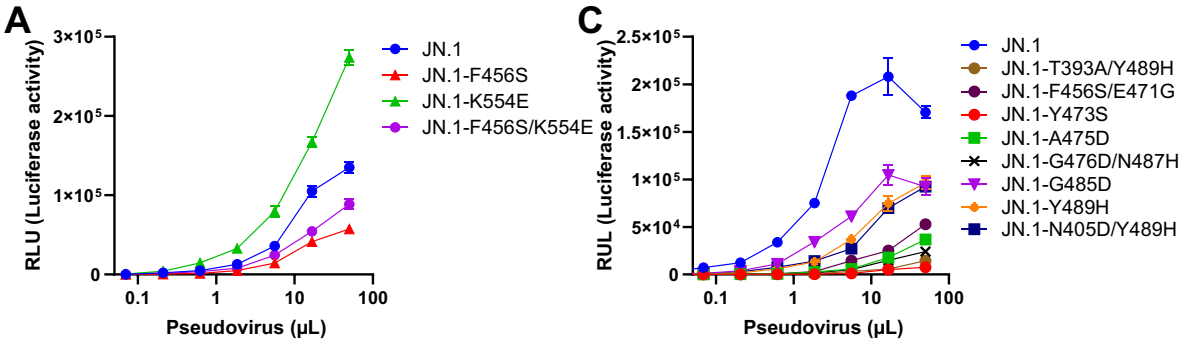

B

Neutralization (IC_{50}, μg/mL)	19-77	19-77ΔV	hACE2
JN.1	0.101	0.013	0.315
JN.1-E554K	0.104	0.009	0.167
JN.1-F456S	>10	0.675	0.304
JN.1-F456S/K554E	>10	0.424	0.695

<0.01	0.01-0.1	0.1-1	1-10	>10

D

Neutralization (IC_{50}, μg/mL)	19-77	19-77ΔA	19-77ΔL	19-77ΔV	hACE2
JN.1	0.047	0.008	0.009	0.008	0.088
JN.1-T393A/Y489H	>10	>10	>10	>10	>10
JN.1-F456S/E471G	>10	>10	>10	>10	9.039
JN.1-Y473S	>10	>10	>10	>10	>10
JN.1-A475D	>10	>10	>10	>10	>10
JN.1-G476D/N487H	>10	>10	>10	>10	>10
JN.1-G485D	>10	0.074	0.113	0.084	1.094
JN.1-Y489H	>10	0.363	0.519	0.976	2.345
JN.1-N405D/Y489H	>10	>10	>10	>10	2.967

Figure S7. Infectivity and neutralization activity of 19-77ΔV escape variants in the context of VSV pseudotyped viruses.

A. Infectivity of the indicated pseudotyped escape variants selected by 19-77ΔV from authentic JN.1 in Vero-E6-TMPRSS2-T2A-ACE2 cells. Data are shown as mean ± SEM (standard error of the mean).

B. Infectivity of the indicated pseudotyped escape variants selected by 19-77ΔV from replication-competent VSV-JN.1 in Vero-E6-TMPRSS2-T2A-ACE2 cells. Data are shown as mean ± SEM.

C. Neutralization IC_{50} values of 19-77, 19-77ΔV, and hACE2 against the indicated pseudotyped escape variants.

D. Neutralization IC_{50} values of 19-77, 19-77ΔA/L/V, and hACE2 against the indicated pseudotyped escape variants.

See also **Figure 7**.

STAR METHODS

Key resource table

Resource availability

Lead contact

Materials availability

Data and code availability

Experimental model and subjects

Human subject

Cell lines

Method details

Monoclonal antibodies

Plasmid construction

Protein purification

ELISA

Antibody PK in mice

Pseudovirus production and infectivity

Pseudovirus neutralization assay

Selection of escape mutations

Antigen-specific memory B cell sorting and single-cell B cell receptor sequencing

Identification of spike-specific antibody transcripts

Antibody transcript annotation

Crystallization and Data processing

Cryo-EM sample preparation

Cryo-EM data collection and analysis

Model building and refinement

In silico antibody engineering

Molecular dynamics analysis

Structure comparison analysis

QUANTIFICATION AND STATISTICAL ANALYSIS

ACKNOWLEDGEMENTS

This study was supported by funding from the Gates Foundation (INV019355) and donations from Andrew and Peggy Cherng.

AUTHOR CONTRIBUTIONS

D.D.H. and L.L. conceived this project. J.Y. J.H., and J.T. constructed antibody expression plasmids. R.G.C. conducted cryo-EM and E.R.R. conducted x-ray. J.Y. studied antibody PK in mice. M.S.N. and Y.H. performed escape virus selection on live virus. Y.G. did bioinformatic and structural analyses. Q.W. and L.L. conducted all other experiments

584 including antigen-specific B cell sorting, protein expression plasmid construction, pseudovirus
585 neutralization assays, ELISA, protein/antibody purification, rVSV-JN.1 escape variants
586 selection, etc. L.S., L.L. and D.D.H. directed and supervised the project. Q.W., Y.G., R.G.C.,
587 L.L., L.S., and D.D.H. analyzed the results and wrote the manuscript.
588
589 **DECLARATION OF INTERESTS**
590 Q.W., J.Y., R.G.C. Y.G., L.S., L.L., and D.D.H. are inventors on the patent application (WH
591 Ref: 0019240.01338US1) or the provisional patent application (63/619,716) filed by Columbia
592 University for a number of SARS-CoV-2 neutralizing antibodies described in this manuscript.
593 Both sets of applications are under review. D.D.H. is a co-founder of TaiMed Biologics and
594 RenBio, consultant to WuXi Biologics and Brii Biosciences, and board director for Vicarious
595 Surgical.

596 **REFERENCES**
597

598 1. Wang, P., Nair, M.S., Liu, L., Iketani, S., Luo, Y., Guo, Y., Wang, M., Yu, J., Zhang,
599 B., Kwong, P.D., et al. (2021). Antibody resistance of SARS-CoV-2 variants B.1.351
600 and B.1.1.7. Nature *593*, 130-135. 10.1038/s41586-021-03398-2.
601 2. Cerutti, G., Guo, Y., Zhou, T., Gorman, J., Lee, M., Rapp, M., Reddem, E.R., Yu, J.,
602 Bahna, F., Bimela, J., et al. (2021). Potent SARS-CoV-2 neutralizing antibodies
603 directed against spike N-terminal domain target a single supersite. Cell Host Microbe
604 *29*, 819-833 e817. 10.1016/j.chom.2021.03.005.
605 3. McCallum, M., De Marco, A., Lempp, F.A., Tortorici, M.A., Pinto, D., Walls, A.C.,
606 Beltramello, M., Chen, A., Liu, Z., Zatta, F., et al. (2021). N-terminal domain
607 antigenic mapping reveals a site of vulnerability for SARS-CoV-2. Cell *184*, 2332-
608 2347 e2316. 10.1016/j.cell.2021.03.028.
609 4. Wang, P., Casner, R.G., Nair, M.S., Wang, M., Yu, J., Cerutti, G., Liu, L., Kwong,
610 P.D., Huang, Y., Shapiro, L., and Ho, D.D. (2021). Increased resistance of SARS-
611 CoV-2 variant P.1 to antibody neutralization. Cell Host Microbe *29*, 747-751 e744.
612 10.1016/j.chom.2021.04.007.
613 5. Barnes, C.O., Jette, C.A., Abernathy, M.E., Dam, K.A., Esswein, S.R., Gristick, H.B.,
614 Malyutin, A.G., Sharaf, N.G., Huey-Tubman, K.E., Lee, Y.E., et al. (2020). SARS-
615 CoV-2 neutralizing antibody structures inform therapeutic strategies. Nature *588*,
616 682-687. 10.1038/s41586-020-2852-1.
617 6. Planas, D., Veyer, D., Baidaliuk, A., Staropoli, I., Guivel-Benhassine, F., Rajah,
618 M.M., Planchais, C., Porrot, F., Robillard, N., Puech, J., et al. (2021). Reduced
619 sensitivity of SARS-CoV-2 variant Delta to antibody neutralization. Nature *596*, 276-
620 280. 10.1038/s41586-021-03777-9.
621 7. Shi, R., Shan, C., Duan, X., Chen, Z., Liu, P., Song, J., Song, T., Bi, X., Han, C., Wu,
622 L., et al. (2020). A human neutralizing antibody targets the receptor-binding site of
623 SARS-CoV-2. Nature *584*, 120-124. 10.1038/s41586-020-2381-y.
624 8. Jones, B.E., Brown-Augsburger, P.L., Corbett, K.S., Westendorf, K., Davies, J.,
625 Cujec, T.P., Wiethoff, C.M., Blackbourne, J.L., Heinz, B.A., Foster, D., et al. (2021).
626 The neutralizing antibody, LY-CoV555, protects against SARS-CoV-2 infection in
627 nonhuman primates. Sci Transl Med *13*. 10.1126/scitranslmed.abf1906.
628 9. Hansen, J., Baum, A., Pascal, K.E., Russo, V., Giordano, S., Wloga, E., Fulton, B.O.,
629 Yan, Y., Koon, K., Patel, K., et al. (2020). Studies in humanized mice and
630 convalescent humans yield a SARS-CoV-2 antibody cocktail. Science *369*, 1010-
631 1014. 10.1126/science.abd0827.
632 10. Park, Y.J., De Marco, A., Starr, T.N., Liu, Z., Pinto, D., Walls, A.C., Zatta, F.,
633 Zepeda, S.K., Bowen, J.E., Sprouse, K.R., et al. (2022). Antibody-mediated broad
634 sarbecovirus neutralization through ACE2 molecular mimicry. Science *375*, 449-454.
635 10.1126/science.abm8143.
636 11. Shu, Y., and McCauley, J. (2017). GISAID: Global initiative on sharing all influenza
637 data - from vision to reality. Euro Surveill *22*. 10.2807/1560-
638 7917.ES.2017.22.13.30494.
639 12. Scott, L., Hsiao, N.Y., Moyo, S., Singh, L., Tegally, H., Dor, G., Maes, P., Pybus,
640 O.G., Kraemer, M.U.G., Semenova, E., et al. (2021). Track Omicron's spread with
641 molecular data. Science *374*, 1454-1455. 10.1126/science.abn4543.
642 13. Liu, L., Iketani, S., Guo, Y., Chan, J.F., Wang, M., Liu, L., Luo, Y., Chu, H., Huang,
643 Y., Nair, M.S., et al. (2022). Striking antibody evasion manifested by the Omicron
644 variant of SARS-CoV-2. Nature *602*, 676-681. 10.1038/s41586-021-04388-0.

14. Carreno, J.M., Alshammary, H., Tcheou, J., Singh, G., Raskin, A.J., Kawabata, H., Sominsky, L.A., Clark, J.J., Adelsberg, D.C., Bielak, D.A., et al. (2022). Activity of convalescent and vaccine serum against SARS-CoV-2 Omicron. Nature *602*, 682-688. 10.1038/s41586-022-04399-5.
15. Cameroni, E., Bowen, J.E., Rosen, L.E., Saliba, C., Zepeda, S.K., Culap, K., Pinto, D., VanBlargan, L.A., De Marco, A., di Iulio, J., et al. (2022). Broadly neutralizing antibodies overcome SARS-CoV-2 Omicron antigenic shift. Nature *602*, 664-670. 10.1038/s41586-021-04386-2.
16. Planas, D., Saunders, N., Maes, P., Guivel-Benhassine, F., Planchais, C., Buchrieser, J., Bolland, W.H., Porrot, F., Staropoli, I., Lemoine, F., et al. (2022). Considerable escape of SARS-CoV-2 Omicron to antibody neutralization. Nature *602*, 671-675. 10.1038/s41586-021-04389-z.
17. Cao, Y., Wang, J., Jian, F., Xiao, T., Song, W., Yisimayi, A., Huang, W., Li, Q., Wang, P., An, R., et al. (2022). Omicron escapes the majority of existing SARS-CoV-2 neutralizing antibodies. Nature *602*, 657-663. 10.1038/s41586-021-04385-3.
18. Cele, S., Jackson, L., Khoury, D.S., Khan, K., Moyo-Gwete, T., Tegally, H., San, J.E., Cromer, D., Scheepers, C., Amoako, D.G., et al. (2022). Omicron extensively but incompletely escapes Pfizer BNT162b2 neutralization. Nature *602*, 654-656. 10.1038/s41586-021-04387-1.
19. Zost, S.J., Gilchuk, P., Case, J.B., Binshtein, E., Chen, R.E., Nkolola, J.P., Schafer, A., Reidy, J.X., Trivette, A., Nargi, R.S., et al. (2020). Potently neutralizing and protective human antibodies against SARS-CoV-2. Nature *584*, 443-449. 10.1038/s41586-020-2548-6.
20. Wang, Q., Guo, Y., Iketani, S., Nair, M.S., Li, Z., Mohri, H., Wang, M., Yu, J., Bowen, A.D., Chang, J.Y., et al. (2022). Antibody evasion by SARS-CoV-2 Omicron subvariants BA.2.12.1, BA.4 and BA.5. Nature *608*, 603-608. 10.1038/s41586-022-05053-w.
21. Wang, Q., Iketani, S., Li, Z., Liu, L., Guo, Y., Huang, Y., Bowen, A.D., Liu, M., Wang, M., Yu, J., et al. (2023). Alarming antibody evasion properties of rising SARS-CoV-2 BQ and XBB subvariants. Cell *186*, 279-286 e278. 10.1016/j.cell.2022.12.018.
22. Pinto, D., Park, Y.J., Beltramello, M., Walls, A.C., Tortorici, M.A., Bianchi, S., Jaconi, S., Culap, K., Zatta, F., De Marco, A., et al. (2020). Cross-neutralization of SARS-CoV-2 by a human monoclonal SARS-CoV antibody. Nature *583*, 290-295. 10.1038/s41586-020-2349-y.
23. Westendorf, K., Zentelis, S., Wang, L., Foster, D., Vaillancourt, P., Wiggin, M., Lovett, E., van der Lee, R., Hendle, J., Pustilnik, A., et al. (2022). LY-CoV1404 (bebtelovimab) potently neutralizes SARS-CoV-2 variants. Cell Rep *39*, 110812. 10.1016/j.celrep.2022.110812.
24. Wang, Q., Guo, Y., Zhang, R.M., Ho, J., Mohri, H., Valdez, R., Manthei, D.M., Gordon, A., Liu, L., and Ho, D.D. (2023). Antibody neutralisation of emerging SARS-CoV-2 subvariants: EG.5.1 and XBC.1.6. Lancet Infect Dis *23*, e397-e398. 10.1016/S1473-3099(23)00555-8.
25. Yue, C., Song, W., Wang, L., Jian, F., Chen, X., Gao, F., Shen, Z., Wang, Y., Wang, X., and Cao, Y. (2023). ACE2 binding and antibody evasion in enhanced transmissibility of XBB.1.5. Lancet Infect Dis *23*, 278-280. 10.1016/S1473-3099(23)00010-5.
26. Jian, F., Feng, L., Yang, S., Yu, Y., Wang, L., Song, W., Yisimayi, A., Chen, X., Xu, Y., Wang, P., et al. (2023). Convergent evolution of SARS-CoV-2 XBB lineages on

694 receptor-binding domain 455-456 synergistically enhances antibody evasion and
695 ACE2 binding. PLoS Pathog *19*, e1011868. 10.1371/journal.ppat.1011868.
696 27. Wang, Q., Guo, Y., Liu, L., Schwanz, L.T., Li, Z., Nair, M.S., Ho, J., Zhang, R.M.,
697 Iketani, S., Yu, J., et al. (2023). Antigenicity and receptor affinity of SARS-CoV-2
698 BA.2.86 spike. Nature. 10.1038/s41586-023-06750-w.
699 28. Hong, Q., Han, W., Li, J., Xu, S., Wang, Y., Xu, C., Li, Z., Wang, Y., Zhang, C.,
700 Huang, Z., and Cong, Y. (2022). Molecular basis of receptor binding and antibody
701 neutralization of Omicron. Nature *604*, 546-552. 10.1038/s41586-022-04581-9.
702 29. Guenthoer, J., Lilly, M., Starr, T.N., Dadonaite, B., Lovendahl, K.N., Croft, J.T.,
703 Stoddard, C.I., Chohan, V., Ding, S., Ruiz, F., et al. (2023). Identification of broad,
704 potent antibodies to functionally constrained regions of SARS-CoV-2 spike following
705 a breakthrough infection. Proc Natl Acad Sci U S A *120*, e2220948120.
706 10.1073/pnas.2220948120.
707 30. Liu, L., Casner, R.G., Guo, Y., Wang, Q., Iketani, S., Chan, J.F., Yu, J., Dadonaite,
708 B., Nair, M.S., Mohri, H., et al. (2023). Antibodies targeting a quaternary site on
709 SARS-CoV-2 spike glycoprotein prevent viral receptor engagement by
710 conformational locking. Immunity *56*, 2442-2455 e2448.
711 10.1016/j.immuni.2023.09.003.
712 31. Looi, M.K. (2023). Covid-19: WHO adds JN.1 as new variant of interest. BMJ *383*,
713 2975. 10.1136/bmj.p2975.
714 32. Wang, Q., Guo, Y., Bowen, A., Mellis, I.A., Valdez, R., Gherasim, C., Gordon, A.,
715 Liu, L., and Ho, D.D. (2024). XBB.1.5 monovalent mRNA vaccine booster elicits
716 robust neutralizing antibodies against XBB subvariants and JN.1. Cell Host Microbe
717 *32*, 315-321 e313. 10.1016/j.chom.2024.01.014.
718 33. FDA (2024). FDA Roundup: March 22, 2024. https://www.fda.gov/news-
719 events/press-announcements/fda-roundup-march-22-2024.
720 34. Wang, Q., Guo, Y., Mellis, I.A., Wu, M., Mohri, H., Gherasim, C., Valdez, R.,
721 Purpura, L.J., Yin, M.T., Gordon, A., and Ho, D.D. (2024). Antibody evasiveness of
722 SARS-CoV-2 subvariants KP.3.1.1 and XEC. bioRxiv, 2024.2011.2017.624037.
723 10.1101/2024.11.17.624037.
724 35. Wang, Q., Guo, Y., Ho, J., and Ho, D.D. (2024). Activity of Research-Grade
725 Pemivibart against Recent SARS-CoV-2 JN.1 Sublineages. N Engl J Med *391*, 1863-
726 1864. 10.1056/NEJMc2410203.
727 36. Liu, L., Wang, P., Nair, M.S., Yu, J., Rapp, M., Wang, Q., Luo, Y., Chan, J.F., Sahi,
728 V., Figueroa, A., et al. (2020). Potent neutralizing antibodies against multiple epitopes
729 on SARS-CoV-2 spike. Nature *584*, 450-456. 10.1038/s41586-020-2571-7.
730 37. Yuan, M., Liu, H., Wu, N.C., Lee, C.D., Zhu, X., Zhao, F., Huang, D., Yu, W., Hua,
731 Y., Tien, H., et al. (2020). Structural basis of a shared antibody response to SARS-
732 CoV-2. Science *369*, 1119-1123. 10.1126/science.abd2321.
733 38. Schymkowitz, J., Borg, J., Stricher, F., Nys, R., Rousseau, F., and Serrano, L. (2005).
734 The FoldX web server: an online force field. Nucleic Acids Res *33*, W382-388.
735 10.1093/nar/gki387.
736 39. Fenwick, C., Turelli, P., Duhoo, Y., Lau, K., Herate, C., Marlin, R., Lamrayah, M.,
737 Campos, J., Esteves-Leuenberger, L., Farina, A., et al. (2023). Broadly potent anti-
738 SARS-CoV-2 antibody shares 93% of epitope with ACE2 and provides full protection
739 in monkeys. J Infect *87*, 524-537. 10.1016/j.jinf.2023.10.008.
740 40. Cao, Y., Jian, F., Wang, J., Yu, Y., Song, W., Yisimayi, A., Wang, J., An, R., Chen,
741 X., Zhang, N., et al. (2022). Imprinted SARS-CoV-2 humoral immunity induces
742 convergent Omicron RBD evolution. Nature. 10.1038/s41586-022-05644-7.

41. Nutalai, R., Zhou, D., Tuekprakhon, A., Ginn, H.M., Supasa, P., Liu, C., Huo, J., Mentzer, A.J., Duyvesteyn, H.M.E., Dijokaite-Guraliuc, A., et al. (2022). Potent cross-reactive antibodies following Omicron breakthrough in vaccinees. Cell *185*, 2116-2131 e2118. 10.1016/j.cell.2022.05.014.
42. Cao, Y., Su, B., Guo, X., Sun, W., Deng, Y., Bao, L., Zhu, Q., Zhang, X., Zheng, Y., Geng, C., et al. (2020). Potent Neutralizing Antibodies against SARS-CoV-2 Identified by High-Throughput Single-Cell Sequencing of Convalescent Patients' B Cells. Cell *182*, 73-84 e16. 10.1016/j.cell.2020.05.025.
43. Cao, Y., Jian, F., Zhang, Z., Yisimayi, A., Hao, X., Bao, L., Yuan, F., Yu, Y., Du, S., Wang, J., et al. (2022). Rational identification of potent and broad sarbecovirus-neutralizing antibody cocktails from SARS convalescents. Cell Rep *41*, 111845. 10.1016/j.celrep.2022.111845.
44. Jian, F., Wec, A.Z., Feng, L., Yu, Y., Wang, L., Wang, P., Yu, L., Wang, J., Hou, J., Berrueta, D.M., et al. (2024). A generalized framework to identify SARS-CoV-2 broadly neutralizing antibodies. bioRxiv, 2024.2004.2016.589454. 10.1101/2024.04.16.589454.
45. Rosen, L.E., Tortorici, M.A., De Marco, A., Pinto, D., Foreman, W.B., Taylor, A.L., Park, Y.J., Bohan, D., Rietz, T., Errico, J.M., et al. (2024). A potent pan-sarbecovirus neutralizing antibody resilient to epitope diversification. Cell. 10.1016/j.cell.2024.09.026.
46. Yu, L., Wang, Y., Liu, Y., Xing, X., Li, C., Wang, X., Shi, J., Ma, W., Li, J., Chen, Y., et al. (2024). Potent and broadly neutralizing antibodies against sarbecoviruses elicited by single ancestral SARS-CoV-2 infection. bioRxiv, 2024.2006.2006.597720. 10.1101/2024.06.06.597720.
47. Yao, T., Ma, Z., Lan, K., Guo, Y., and Liu, L. (2024). Neutralizing Activity and Viral Escape of Pemivibart by SARS-CoV-2 JN.1 sublineages. bioRxiv, 2024.2011.2008.622746. 10.1101/2024.11.08.622746.
48. Planas, D., Staropoli, I., Planchais, C., Yab, E., Jeyarajah, B., Rahou, Y., Prot, M., Guivel-Benhassine, F., Lemoine, F., Enouf, V., et al. (2024). Escape of SARS-CoV-2 Variants KP.1.1, LB.1, and KP3.3 From Approved Monoclonal Antibodies. Pathog Immun *10*, 1-11. 10.20411/pai.v10i1.752.
49. Tixagevimab and Cilgavimab (Evusheld) for Pre-Exposure Prophylaxis of COVID-19. (2022). JAMA *327*, 384-385. 10.1001/jama.2021.24931.
50. Marks, J.D., Griffiths, A.D., Malmqvist, M., Clackson, T.P., Bye, J.M., and Winter, G. (1992). By-passing immunization: building high affinity human antibodies by chain shuffling. Biotechnology (N Y) *10*, 779-783. 10.1038/nbt0792-779.
51. Yoshinaga, K., Matsumoto, M., Torikai, M., Sugyo, K., Kuroki, S., Nogami, K., Matsumoto, R., Hashiguchi, S., Ito, Y., Nakashima, T., and Sugimura, K. (2008). Ig L-chain shuffling for affinity maturation of phage library-derived human anti-human MCP-1 antibody blocking its chemotactic activity. J Biochem *143*, 593-601. 10.1093/jb/mvn009.
52. Kim, H.Y., Stojadinovic, A., and Izadjoo, M.J. (2014). Affinity maturation of monoclonal antibodies by multi-site-directed mutagenesis. Methods Mol Biol *1131*, 407-420. 10.1007/978-1-62703-992-5_24.
53. Banach, B.B., Pletnev, S., Olia, A.S., Xu, K., Zhang, B., Rawi, R., Bylund, T., Doria-Rose, N.A., Nguyen, T.D., Fahad, A.S., et al. (2023). Antibody-directed evolution reveals a mechanism for enhanced neutralization at the HIV-1 fusion peptide site. Nat Commun *14*, 7593. 10.1038/s41467-023-42098-5.
54. Pan, Y., Du, J., Liu, J., Wu, H., Gui, F., Zhang, N., Deng, X., Song, G., Li, Y., Lu, J., et al. (2021). Screening of potent neutralizing antibodies against SARS-CoV-2 using

793 convalescent patients-derived phage-display libraries. Cell Discov *7*, 57.
794 10.1038/s41421-021-00295-w.
795 55. Hess, G.T., Fresard, L., Han, K., Lee, C.H., Li, A., Cimprich, K.A., Montgomery,
796 S.B., and Bassik, M.C. (2016). Directed evolution using dCas9-targeted somatic
797 hypermutation in mammalian cells. Nat Methods *13*, 1036-1042.
798 10.1038/nmeth.4038.
799 56. Mason, D.M., Weber, C.R., Parola, C., Meng, S.M., Greiff, V., Kelton, W.J., and
800 Reddy, S.T. (2018). High-throughput antibody engineering in mammalian cells by
801 CRISPR/Cas9-mediated homology-directed mutagenesis. Nucleic Acids Res *46*,
802 7436-7449. 10.1093/nar/gky550.
803 57. Wellner, A., McMahon, C., Gilman, M.S.A., Clements, J.R., Clark, S., Nguyen, K.M.,
804 Ho, M.H., Hu, V.J., Shin, J.E., Feldman, J., et al. (2021). Rapid generation of potent
805 antibodies by autonomous hypermutation in yeast. Nat Chem Biol *17*, 1057-1064.
806 10.1038/s41589-021-00832-4.
807 58. Desautels, T.A., Arrildt, K.T., Zemla, A.T., Lau, E.Y., Zhu, F., Ricci, D., Cronin, S.,
808 Zost, S.J., Binshtein, E., Scheaffer, S.M., et al. (2024). Computationally restoring the
809 potency of a clinical antibody against Omicron. Nature *629*, 878-885.
810 10.1038/s41586-024-07385-1.
811 59. Shan, S., Luo, S., Yang, Z., Hong, J., Su, Y., Ding, F., Fu, L., Li, C., Chen, P., Ma, J.,
812 et al. (2022). Deep learning guided optimization of human antibody against SARS-
813 CoV-2 variants with broad neutralization. Proc Natl Acad Sci U S A *119*,
814 e2122954119. 10.1073/pnas.2122954119.
815 60. Li, L., Gupta, E., Spaeth, J., Shing, L., Jaimes, R., Engelhart, E., Lopez, R., Caceres,
816 R.S., Bepler, T., and Walsh, M.E. (2023). Machine learning optimization of candidate
817 antibody yields highly diverse sub-nanomolar affinity antibody libraries. Nat
818 Commun *14*, 3454. 10.1038/s41467-023-39022-2.
819 61. Burn Aschner, C., Muthuraman, K., Kucharska, I., Cui, H., Prieto, K., Nair, M.S.,
820 Wang, M., Huang, Y., Christie-Holmes, N., Poon, B., et al. (2023). A multi-specific,
821 multi-affinity antibody platform neutralizes sarbecoviruses and confers protection
822 against SARS-CoV-2 in vivo. Sci Transl Med *15*, eadf4549.
823 10.1126/scitranslmed.adf4549.
824 62. Song, R., Oren, D.A., Franco, D., Seaman, M.S., and Ho, D.D. (2013). Strategic
825 addition of an N-linked glycan to a monoclonal antibody improves its HIV-1-
826 neutralizing activity. Nat Biotechnol *31*, 1047-1052. 10.1038/nbt.2677.
827 63. Ovchinnikov, V., Louveau, J.E., Barton, J.P., Karplus, M., and Chakraborty, A.K.
828 (2018). Role of framework mutations and antibody flexibility in the evolution of
829 broadly neutralizing antibodies. Elife *7*. 10.7554/eLife.33038.
830 64. Tramontano, A., Chothia, C., and Lesk, A.M. (1990). Framework residue 71 is a
831 major determinant of the position and conformation of the second hypervariable
832 region in the VH domains of immunoglobulins. J Mol Biol *215*, 175-182.
833 10.1016/S0022-2836(05)80102-0.
834 65. Yanaka, S., Moriwaki, Y., Tsumoto, K., and Sugase, K. (2017). Elucidation of
835 potential sites for antibody engineering by fluctuation editing. Sci Rep *7*, 9597.
836 10.1038/s41598-017-10246-9.
837 66. Liu, L., Iketani, S., Guo, Y., Reddem, E.R., Casner, R.G., Nair, M.S., Yu, J., Chan,
838 J.F., Wang, M., Cerutti, G., et al. (2022). An antibody class with a common CDRH3
839 motif broadly neutralizes sarbecoviruses. Sci Transl Med *14*, eabn6859.
840 10.1126/scitranslmed.abn6859.
841 67. Hsieh, C.L., Goldsmith, J.A., Schaub, J.M., DiVenere, A.M., Kuo, H.C., Javanmardi,
842 K., Le, K.C., Wrapp, D., Lee, A.G., Liu, Y., et al. (2020). Structure-based design of

843 prefusion-stabilized SARS-CoV-2 spikes. Science *369*, 1501-1505.
844 10.1126/science.abd0826.
845 68. Chan, K.K., Dorosky, D., Sharma, P., Abbasi, S.A., Dye, J.M., Kranz, D.M., Herbert,
846 A.S., and Procko, E. (2020). Engineering human ACE2 to optimize binding to the
847 spike protein of SARS coronavirus 2. Science *369*, 1261-1265.
848 10.1126/science.abc0870.
849 69. Kabsch, W. (2010). Integration, scaling, space-group assignment and post-refinement.
850 Acta Crystallogr D Biol Crystallogr *66*, 133-144. 10.1107/S0907444909047374.
851 70. Evans, P.R., and Murshudov, G.N. (2013). How good are my data and what is the
852 resolution? Acta Crystallogr D Biol Crystallogr *69*, 1204-1214.
853 10.1107/S0907444913000061.
854 71. Winn, M.D., Ballard, C.C., Cowtan, K.D., Dodson, E.J., Emsley, P., Evans, P.R.,
855 Keegan, R.M., Krissinel, E.B., Leslie, A.G., McCoy, A., et al. (2011). Overview of
856 the CCP4 suite and current developments. Acta Crystallogr D Biol Crystallogr *67*,
857 235-242. 10.1107/S0907444910045749.
858 72. McCoy, A.J. (2007). Solving structures of protein complexes by molecular
859 replacement with Phaser. Acta Crystallogr D Biol Crystallogr *63*, 32-41.
860 10.1107/S0907444906045975.
861 73. Emsley, P., and Cowtan, K. (2004). Coot: model-building tools for molecular
862 graphics. Acta Crystallogr D Biol Crystallogr *60*, 2126-2132.
863 10.1107/S0907444904019158.
864 74. Adams, P.D., Afonine, P.V., Bunkoczi, G., Chen, V.B., Davis, I.W., Echols, N.,
865 Headd, J.J., Hung, L.W., Kapral, G.J., Grosse-Kunstleve, R.W., et al. (2010).
866 PHENIX: a comprehensive Python-based system for macromolecular structure
867 solution. Acta Crystallogr D Biol Crystallogr *66*, 213-221.
868 10.1107/S0907444909052925.
869 75. Davis, I.W., Murray, L.W., Richardson, J.S., and Richardson, D.C. (2004).
870 MOLPROBITY: structure validation and all-atom contact analysis for nucleic acids
871 and their complexes. Nucleic Acids Res *32*, W615-619. 10.1093/nar/gkh398.
872 76. Jumper, J., Evans, R., Pritzel, A., Green, T., Figurnov, M., Ronneberger, O.,
873 Tunyasuvunakool, K., Bates, R., Zidek, A., Potapenko, A., et al. (2021). Highly
874 accurate protein structure prediction with AlphaFold. Nature *596*, 583-589.
875 10.1038/s41586-021-03819-2.
876 77. Meng, E.C., Goddard, T.D., Pettersen, E.F., Couch, G.S., Pearson, Z.J., Morris, J.H.,
877 and Ferrin, T.E. (2023). UCSF ChimeraX: Tools for structure building and analysis.
878 Protein Sci *32*, e4792. 10.1002/pro.4792.
879 78. Liebschner, D., Afonine, P.V., Baker, M.L., Bunkoczi, G., Chen, V.B., Croll, T.I.,
880 Hintze, B., Hung, L.W., Jain, S., McCoy, A.J., et al. (2019). Macromolecular
881 structure determination using X-rays, neutrons and electrons: recent developments in
882 Phenix. Acta Crystallogr D Struct Biol *75*, 861-877. 10.1107/S2059798319011471.

883

STAR METHODS

RESOURCE AVALIABLILITY

Lead contact

Further information and requests for resources should be directed to and will be fulfilled by the lead contact, David D. Ho (dh2994@cumc.columbia.edu).

Materials availability

All requests for resources and reagents should be directed to and will be fulfilled by the Lead Contact, David D. Ho (dh2994@cumc.columbia.edu). This includes selective cell lines, plasmids, antibodies, viruses, serum, and proteins. All reagents will be made available on request after completion of a Material Transfer Agreement.

Data and code availability

• Data

Data reported in this paper will be shared by the lead contact upon request.

• Code

This paper does not report original code.

• All other items

Any additional information required to reanalyze the data reported in this paper is available from the lead contact upon request.

EXPERIMENTAL MODEL AND SUBJECTS

Human subject

Blood sample from Donor 19, a 41-year-old Asian male, was collected at Columbia University Irving Medical Center. Donor 19 was confirmed for a BA.5 infection by PCR sequencing (Single Nucleotide Polymorphisms) and provided written informed consent. Sample collections were performed under protocols reviewed and approved by the Institutional Review Board of Columbia University. Clinical information of Donor 19 is provided in **Figure S1A**.

Cell lines

Vero-E6 (CRL-1586) and HEK293T (CRL-3216) cells were purchased from the American Type Culture Collection (ATCC). Expi293 cells (A14527) were purchased from Thermo Fisher Scientific. Vero-E6-TMPRSS2-T2A-ACE2 (NR-54970) were obtained from BEI Resources. 293T-ACE2 were kindly provided by Dr. Jesse D. Bloom. Morphology of each cell line was confirmed visually before use. All cell lines tested mycoplasma negative. Vero-E6 and Vero-E6-TMPRSS2-T2A-ACE2 cell lines are from African green monkey kidneys. HEK293T, 293T-ACE2, and Expi293 cells are of female origin.

METHOD DETAILS

Plasmid construction

928 SARS-CoV-2 spike-expressing plasmids for D614G, Alpha, Beta, Gamma, Delta and Omicron
929 were previously generated[13,20,21,27]. Expressing constructs for the spike proteins of SARS-
930 CoV-2-like sarbecoviruses were either previously generated[66] or newly generated by
931 synthesizing (GenScript) spike genes and then cloned into the pCMV3 vector. To generate the
932 expression constructs for soluble spike trimer (S2P) proteins, the ectodomains (1-1208aa,
933 numbering based on WA1) of the spikes were PCR amplified and cloned into the paH vector
934 and then introduced K986P and V987P substitutions, as well as a "GSAS" substitution of the
935 furin cleavage site (682-685aa in WA1) into the spikes[67]. SARS-CoV S2P was fused with an
936 AVI tag at the C terminus and D614G and XBB.1.5 S2P spikes were tagged with a 6×His tail
937 also at the C terminus. To make SARS-CoV-2 RBD-expressing construct, RBD region (319-
938 537aa) of each variant was fused with a 6×His tag and then cloned into the p3BNC vector. All
939 constructs were confirmed by Sanger sequencing.
940
941 Antibody expressing constructs were generated as previously described[36]. The variable regions
942 of heavy and light chains for each antibody were synthesized (GenScript) and then cloned into
943 the gWiz vector. To make spike/antibody plasmid constructs carrying individual mutations,
944 the Q5® Site-Directed Mutagenesis Kit (NEB) was utilized following the manufacturer's
945 instructions.
946
947 **Protein purification**
948 To make human ACE2-Fc (hACE2) protein, pcDNA3-sACE2-WT(732)-IgG1[68] (Addgene
949 plasmid #154104, gift of Erik Procko) plasmid was transfected into Expi293 cells using 1
950 mg/mL polyethyleneimine (PEI) at a ratio of 1:3, and the supernatants were collected after five
951 days. hACE2 was purified from the cell supernatant by using rProtein A Sepharose (GE). For
952 antibody purification, both heavy and light chains of each antibody were transfected at a ratio
953 of 1:1 into Expi293 cells using PEI. And the expressed antibody in the cell supernatant was
954 purified using the same method as for hACE2 purification. For the spike trimer proteins or
955 RBD proteins, paH-spike or p3BNC-RBD, respectively, was transfected into Expi293 cells
956 using PEI at a ratio of 1:3, and the supernatants were collected five days later. The His tagged
957 and the AVI tagged proteins were purified using Excel resin (Cytiva) and Agarose bound
958 Galanthus nivalis lectin (VectorLabs, AL-1243-5) according to the manufacturers' instructions.
959 The molecular weight and purity were checked by running the proteins on SDS-PAGE.
960
961 After purification of 19-77 and 19-77ΔA/L/V, 100 µg of each antibody was prepared and run
962 through a Superdex 200 Increase 10/300 GL column to generate their size exclusion
963 chromatography (SEC) profiles. AVI tagged SARS-CoV S2P protein were biotinylated using
964 the BirA biotin-protein ligase standard reaction kit (Avidity LLC; BirA500) following the
965 manufacturer's instructions.
966
967 **ELISA**
968 50 ng per well of an antigen such as S2P spike, NTD (ACROBiosystems, S1D-C52H6), RBD
969 (ACROBiosystems, SPD-C52H1), RBD-SD1 (Exonbio, 19Cov-S130), S1 (ACROBiosystems,
970 S1N-C52H3), or S2 (ACROBiosystems, S2N-C52H2) was coated onto ELISA plates at 4°C
971 overnight. The ELISA plates were then blocked with 300 µL of blocking buffer consisting of

phosphate-buffered saline (PBS) with 1% bovine serum albumin and 20% bovine calf serum (Sigma-Aldrich) at 37°C for 2 hours. Afterwards, 100 µL of 5-fold serially diluted antibodies was added and then incubated at 37°C for 1 hour. Next, 100 µL of 10,000-fold diluted Peroxidase AffiniPure goat anti-human IgG Fcγ fragment-specific antibody (Jackson ImmunoResearch, catalog no. 109-035-170, RRID: AB_2810887) was added into each well and incubated for another 1 hour at 37°C. The plates were washed between each step with PBST (0.5% Tween-20 in PBS). Last, 3,3′,5,5′-tetramethylbenzidine (TMB) substrate (Sigma-Aldrich) was added and incubated before the reaction was stopped using 1 M sulfuric acid. Absorbance was measured at 450 nm.

Antibody pharmacokinetics in mice

100 µg (1 mg/mL) of each antibody was intraperitoneally (ip) injected into Balb C mice (3 mice for each antibody). Mouse blood was collected on day 2, 4, 7 and 10 post ip injection and antibody concentrations in serum were measured by ELISA. Briefly, 100 ng goat anti-human IgG Fc antibody (Cat: 109-005-008, JacksonImmunoResearch) was coated per well in 96-well plates overnight and the ELISA plates were then blocked with 300 µL of blocking buffer consisting of PBS with 1% bovine serum albumin and 20% bovine calf serum (Sigma-Aldrich) at 37°C for 2 hours. Afterwards, 100 µL of 3-fold serially diluted serum or 2-fold serially diluted purified antibody was added and then incubated at 37°C for 1 hour. Next, 100 µL of 10,000-fold diluted Peroxidase AffiniPure goat anti-human IgG H+L HRP (Cat: 109-035-088, JacksonImmunoResearch) was added into each well and incubated for another 1 hour at 37°C. The plates were washed between each step with PBST (0.5% Tween-20 in PBS). Last, TMB substrate (Sigma-Aldrich) was added and incubated before the reaction was stopped using 1 M sulfuric acid. Absorbance was measured at 450 nm.

Pseudovirus production and infectivity

SARS-CoV-2 pseudoviruses were generated as previously described[36]. In brief, HEK293T cells were transfected with a spike-expressing construct using 1 mg/mL PEI and then infected with VSV-G pseudotyped ΔG-luciferase (G*ΔG-luciferase, Kerafast) one day post-transfection. Two hours after infection, cells were washed three times with PBS, changed to fresh medium, and then cultured for one more day before the cell supernatants were harvested. Pseudoviruses in the cell supernatants were clarified by centrifugation, aliquoted, and stored at -80°C.

To evaluate the infectivity of the pseudotyped escape variants of 19-77 and 19-77ΔV, fresh pseudoviruses without freezing and thawing were serially titrated from 50 µL with a dilution factor of 3 and then inoculated into Vero-E6 cells. After overnight culture, Vero-E6 cells were harvested and quantified for luciferase activity using the Luciferase Assay System (Promega).

Pseudovirus neutralization assay

To normalize the viral input between assays before conducting the neutralization assays, pseudoviruses of SARS-CoV and SARS-CoV-2 variants and SARS-CoV-2-like sarbecoviruses were titrated on Vero-E6 cells and 293T-ACE2 cells. Heat-inactivated serum from Donor 19 was serially diluted starting from 1:25 with a dilution factor of four.

1016 Monoclonal antibodies were 5-fold serially diluted starting from 20 µg/mL in 96 well plates in
1017 triplicate. Then, 50 µL of diluted pseudovirus was added and incubated with 50 µL serial
1018 dilutions of serum or mAb for 1 hour at 37°C. During the co-culture, target cells were
1019 trypsinized, resuspended with fresh medium, and then added into virus-sample mixture at a
1020 density of 4-10 × 10^4 cells/well. The plates were incubated at 37°C for ~12 hours before
1021 luciferase activity was quantified using the Luciferase Assay System (Promega) using SoftMax
1022 Pro v.7.0.2 (Molecular Devices). Neutralization ID_{50} values for sera and IC_{50} values for
1023 antibodies were calculated by fitting a nonlinear five-parameter dose-response curve to the data
1024 in GraphPad Prism v.10.
1025
1026 **Selection of escape mutations.**
1027 SARS-Cov-2 isolate Omicron JN.1 (BEI NR-59693) was mixed with serial five-fold dilutions
1028 of 19-77ΔV antibody at MOI of 0.2 and incubated for 1 h. Following incubation, the mix was
1029 overlaid on a 24-well plate bearing a monolayer of Vero-ACE2-TMPRSS2 cells (BEI NR-
1030 54970) to a final volume of 1 mL. Plates were incubated at 37°C/ 5% CO_2 for 70 h till
1031 cytopathic effect (CPE) was complete (100%) in virus control wells bearing no antibody. At
1032 this time, all wells with antibody dilutions were scored to determine the 50% inhibition titer
1033 (EC_{50}) and supernatant collected from this well was used for subsequent round of selection.
1034 Passaging of the progeny over new Vero-ACE2-TMPRSS2 cells continued till each of the virus
1035 variant was able to form CPE in the presence of 50 µg/mL of the antibody. The resulting
1036 supernatant was then collected, and RNA was extracted using QiaAMP Viral RNA kit (Qiagen
1037 57704). cDNA was obtained using Superscript IV enzyme (Thermo Scientific 18090010).
1038 Spike gene from the cDNA was amplified using limiting dilution nested PCR and sequenced
1039 using Sanger sequencing (Genewiz). Multiple clones from limiting dilution nested PCR were
1040 sequenced to confirm the dominant mutants in the pool of the resulting progeny viruses and a
1041 percentage of their prevalence was calculated from the total number sequenced. At least 8
1042 clones were sequenced from each of the passages reported in **Figure 7**.
1043
1044 To generate recombinant replication-competent VSV-ΔG bearing the JN.1 spike protein (VSV-
1045 ΔG-JN.1), the pVSVΔG-SARS-CoV-2-S_nLucP plasmid was purchased from Kerafast (Cat#
1046 EGA292) and its encoding SARS-CoV-2-S gene was replaced with JN.1 spike gene to create
1047 pVSVΔG-JN.1_nLucP. The pVSVΔG-JN.1_nLucP plasmid and a set of helper plasmids,
1048 including VSV-N, VSV-P, VSV-L, and VSV-G (Kerafast, Cat# EH1012), were then
1049 transfected into 293T cells at a ratio of 5:3:5:1:8 using 1 mg/mL PEI-MAX. Before
1050 transfection, 293T cells were rinsed with serum-free DMEM, incubated with Vaccinia vTF7-3
1051 (Imanis Life Sciences, Cat# REA006) at a MOI of 5 for 45 minutes, and then replaced with
1052 fresh medium. Two days post-transfection, the supernatant was harvested and filtered through
1053 a 0.22 µm filter to remove cell debris and Vaccinia vTF7-3. The rVSV-ΔG-JN.1 generated
1054 from 293T cells was then serially diluted with a dilution factor of 5 and inoculated into Vero-
1055 E6-TMPRSS2-T2A-ACE2 cells in 24-well plates for 1 hour. The virus was then washed away,
1056 and the cells were cultured at 37°C/5% CO_2 for 16-24 hours. Vero-E6-TMPRSS2-T2A-ACE2
1057 cells were monitored, and the virus was harvested from wells in which only one plaque was
1058 observed, then filtered and stored at -80°C. The rVSV-ΔG-JN.1 generated from Vero-E6-
1059 TMPRSS2-T2A-ACE2 cells was titrated on Vero-E6-TMPRSS2-T2A-ACE2 cells before use.

1060 To select escape viruses, rVSVΔG-JN.1 was incubated with 0.4 μg/mL of 19-77ΔV for 1 hour
1061 before being added to Vero-E6-TMPRSS2-T2A-ACE2 cells in 24-well plates at a MOI of 0.01.
1062 A total of 66 replicates were set up. Two days after coculture, cell supernatants from wells
1063 with CPE were harvested, and 100 μL of each supernatant was incubated with 4 μg/mL of 19-
1064 77ΔV for 1 hour before another round of infection in pre-seeded Vero-E6-TMPRSS2-T2A-
1065 ACE2 cells in 24-well plates. Two days later, supernatants containing escape viruses were
1066 further harvested and selected the same way using 20 μg/mL, and then 50 μg/mL, of 19-77ΔV
1067 in a stepwise manner. mRNAs of the escape viruses in the supernatants were then extracted
1068 using the viral RNA/DNA purification kit (MACHEREY-NAGEL, Cat# 740643) and reverse-
1069 transcribed to cDNA using the SuperScript™ VILO™ cDNA Synthesis Kit (Invitrogen, Cat#
1070 11754). The RBD genes of the escape viruses were then amplified using primers 5'-
1071 GGGCATCTACCAGACCAGCAACTTCA-3' and 5'-
1072 GAACACATTGCTGCCTGTGCTGT-3' and sequenced.
1073
1074 **Antigen-specific memory B cell sorting and single-cell B cell receptor sequencing**
1075 Peripheral blood mononuclear cells from Donor 19, and two healthy donors were stained with
1076 the LIVE/DEAD Fixable Yellow Dead Cell Stain Kit (Invitrogen) at ambient temperature for
1077 20 min, followed by washing with RPMI 1640 complete medium [RPMI 1640 + 10% fetal
1078 bovine serum (FBS) + penicillin/streptomycin (P/S) (100 U/mL)] and incubation with 10
1079 μg/mL XBB.1.5 S2P protein and biotinylated SARS-CoV S2P at 4°C for 45 min. Afterwards,
1080 the cells were washed again and incubated with a cocktail of flow cytometry and Hashtag
1081 antibodies, consisting of CD3 PerCP-Cy5.5, CD19 APC/Cyanine 7, CD27 APC, IgM FITC,
1082 anti-His PE/DazzleTM 594, Streptavidin BV421, and human Hashtag 3 at 4°C for 1 hour.
1083 Stained cells were then washed, resuspended in RPMI 1640 complete medium, and sorted for
1084 SARS-CoV and/or XBB.1.5 S2P trimer-specific memory B cells
1085 (CD3−CD19+CD27+IgM−antigen+ live single lymphocytes) by flow cytometry. The sorted
1086 cells were mixed with spike-in CD3+ cells and loaded into a 10X Chromium chip of the 5′
1087 Single Cell Immune Profiling Assay (10X Genomics) at the Columbia University Single-Cell
1088 Analysis Core. Library preparation and quality control were performed according to the
1089 manufacturer's protocol and sequenced on a NextSeq 500 sequencer (Illumina).
1090
1091 **Identification of spike-specific antibody transcripts**
1092 Antibody transcripts specific to the XBB.1.5 S2P spike and SARS-CoV spike trimers were
1093 identified following previously established methods[36]. The assembly of full-length antibody
1094 transcripts was performed utilizing the Cell Ranger V(D)J analysis software (version 3.1.0,
1095 10X Genomics), employing default settings with the GRCh38 V(D)J germline sequence
1096 version 2.0.0 as the reference genome. To differentiate between cells captured in the antigen-
1097 specific sorting process and those added as spike-ins, the count module of Cell Ranger was
1098 used to quantify the presence of all hashtag oligonucleotides in each cell based on Next
1099 Generation Sequencing (NGS) raw data. Identification of high-confidence antigen-specific
1100 cells was achieved using the following criteria: 1) A minimum of 100 copies of the antigen-
1101 specific hashtag was required for a cell to be classified as antigen-specific, 2) Given that
1102 hashtags might detach from their original cells and attach to others within the sample, a cell
1103 was considered truly antigen-specific only if the copy number of its specific hashtag was at

1104 least 1.5 times higher than that of any non-specific hashtag present, 3) Cells deemed to be of
1105 low quality were excluded based on the cell quality assessment algorithm used by Cell Ranger,
1106 4) Only cells expressing both productive heavy and light chain antibody gene pairs were
1107 retained, 5) In instances where a cell exhibited more than two transcripts for heavy and/or light
1108 chains, transcripts supported by fewer than three unique molecular identifiers (UMIs) were
1109 discarded, and 6) Cells sharing identical heavy and light chain sequences, potentially indicative
1110 of mRNA contamination, were consolidated into a single cell entry.
1111
1112 **Antibody transcript annotation**
1113 Transcripts specific to the antigen were analyzed and annotated with SONAR version 2.0,
1114 following previously established procedures. Assignment of V(D)J gene segments to each
1115 transcript was conducted via BLASTn, employing specialized parameters against a germline
1116 gene repository sourced from the International ImMunoGeneTics (IMGT) information system
1117 database. The identification of the Complementarity Determining Region 3 (CDR3) utilized
1118 BLAST alignments of the V and J segments, focusing on the conserved second cysteine within
1119 the V segment and the WGXG (for heavy chains) or FGXG (for light chains) motifs in the J
1120 segment, with "X" indicating any amino acid. Isotype determination for heavy chain transcripts
1121 was achieved by analyzing Constant domain 1 (CH1) sequences against a human CH1 gene
1122 database from IMGT, using BLASTn with standard parameters. The CH1 allele presenting the
1123 lowest E-value was selected for precise isotype classification, adhering to a BLAST E-value
1124 cutoff of 10e-6. Transcripts with incomplete V(D)J segments, frameshifts, or extraneous
1125 sequences beyond the V(D)J region were discarded. The filtered transcripts were then aligned
1126 to their corresponding germline V gene using CLUSTALO, and levels of somatic
1127 hypermutation were quantified through the Sievers method. In instances where cells possessed
1128 multiple high-quality heavy or light chains, potentially indicative of doublets, combinations of
1129 all H and L chains were generated.
1130
1131 **Crystallization and Data processing**
1132
1133 19-77 Fab was produced by digestion of IgG with immobilized Endoproteinase Lys-C (Sigma
1134 Aldrich) equilibrated with 25 mM Tris pH 8.5 and 1 mM EDTA for 3 h. The resulting Fab
1135 was further purified from the cleaved Fc domain by cation exchange chromatography. Fab
1136 purity was analyzed by SDS-PAGE and buffer-exchanged into 20 mM Tris, 150 mM, pH 7.4
1137 prior to cryo-EM/Crystallization experiments.
1138
1139 19-77/SARS-CoV-2-RBD and 19-77/EG5.1-CoV-2-RBD complexes were prepared by mixing
1140 each of the protein components at an equimolar concentration and incubating overnight at 4 °C.
1141 Protein complexes were then isolated by gel filtration on a Superdex-200 column (Cytiva, GE
1142 Healthcare). Fractions containing complexes were pooled and concentrated to 12.0 mg/mL in
1143 SEC buffer. Screening for initial crystallization conditions was carried out in 96-well sitting
1144 drop plates using the vapor-diffusion method with a Mosquito crystallization robot (TTP
1145 LabTech) using various commercially available crystallization screens: MSCG-1 (Anthracene),
1146 Proplex and LMB (Molecular dimensions). Diffraction quality crystals were obtained after
1147 seven days in the following condition for 19-77/SARS-CoV-2-RBD: 0.1 M NaCl, 0.1 M Tris

1148 pH 7.5, 12% w/v PEG 4000, and the following condition for 19-77/ EG5.1-CoV-2-RBD: 75%
1149 MPD and 0.1 M HEPES pH 7.5.
1150
1151 Prior to data collection, crystals were cryoprotected with 40% ethylene glycol supplemented
1152 in mother liquor and flash frozen in liquid nitrogen. X-ray diffraction data extending to 2.8 Å
1153 (19-77/SARS-CoV-2-RBD) and 3.2 Å (19-77/ EG5.1-CoV-2-RBD) resolution were collected
1154 at 100 K on beam line 17-ID-1 (AMX) at Brookhaven National Laboratory. Diffraction data
1155 were processed with XDS[69] and scaled using AIMLESS[70] from the CCP4 software suite
1156 (Collaborative Computational Project Number 4, 1994)[71]. Molecular replacement was
1157 performed with PHASER[72], using a previously reported RBD structure (PDB 7L5B) and for
1158 19-77 Fab, heavy chain (PDB 7XIK), light chain (3FIK) used as search models. Manual
1159 rebuilding of the structure using COOT[73] was alternated with refinement using Phenix refine[74].
1160 The Molprobity server was used for structure validation[75] and PyMOL (version 2.1,
1161 Schrödinger, LLC) for structure visualization. A summary of the X-ray data collection and
1162 refinement statistics are shown in **Figure S2**C.
1163
1164 **Cryo-EM sample preparation**
1165 Fab fragments of antibodies were produced by digestion of IgG with immobilized
1166 Endoproteinase Lys-C (Sigma-Aldrich) equilibrated with 25 mM Tris, pH 8.5, and 1 mM
1167 EDTA for 3 h. The resulting Fabs were purified by ion-exchange chromatography on a mono-
1168 Q column.
1169
1170 For the structure of 19-77 bound to D614G spike, the complex was made by mixing purified
1171 SARS-CoV-2 S2P D614G spike protein with Fab in a 1:3 molar ratio (spike protomer:Fab) in
1172 PBS, pH 7.4, such that the final concentration of spike was 1 mg/mL. This mixture was
1173 incubated on ice for 1 h.
1174
1175 For the structures of the ternary complex of 19-77, RBDs, and S309, complexes were made by
1176 mixing purified SARS-CoV-2 RBD with Fabs in a 1:1.2 molar ratio in PBS, pH 7.4, and further
1177 purified using size exclusion chromatography (SEC) using a Superdex 200 Increase column.
1178 The resulting complex peak was then concentrated to 4 mg/mL and held on ice until
1179 vitrification.
1180
1181 Before freezing, 0.005% (w/v) n-Dodecyl β-D-maltoside (DDM) was added to deter preferred
1182 orientation and aggregation during vitrification. Cryo-EM grids were prepared by applying 3
1183 µL of sample to a freshly glow-discharged carbon-coated copper grid (CF 1.2/1.3 300 mesh);
1184 the sample was then vitrified in liquid ethane using a Vitrobot Mark IV with a wait time of 30
1185 s, a blot time of 3 s, and a blot force of 0.
1186
1187 **Cryo-EM data collection and analysis**
1188 Cryo-EM data for single particle analysis were collected at the Columbia Cryo-EM Facility on
1189 a Titan Krios electron microscope operating at 300 kV, equipped with a Gatan K3-BioQuantum
1190 detector and energy filter, using the Leginon7 software package. Exposures were taken at a
1191 magnification of 105,000x (pixel size of 0.83 Å), using a total electron flux of 58 e-/Å2

fractionated over 50 frames with an exposure time of 2.5 s. A random defocus range of -0.8 to -2.0 µm was used.

Data processing was performed using cryoSPARC v3.3.1.8 Raw movies were aligned and dose-weighted using patch motion correction, and the micrograph contrast transfer function (CTF) parameters were estimated using patch CTF estimation. Micrographs were picked using a blob or template picker and an initial particle set was selected using 2D classification. Further heterogenous refinement was used to 3D-classify particles and remove debris. The resulting curated particle sets were corrected for local motion and refined using homogenous refinement. Local refinement was performed for the spike dataset using a mask enveloping the RBD+Fab variable region. The default cryoSPARC auto-sharpened maps were then used to build the models. Cryo-EM data collection and consensus refinements are summarized in **Figure S2**.

Model building and refinement

Initial molecular models for Fabs were generated using Alphafold Multimer[76] using paired heavy and light sequences. An RBD from PDB 7KNI, an RBD-up spike structure, was used as a starting model. For the initial 19-77 structure, the 14-7 structure (PDB 8F89), RBD (PDB 8IOV), and S309 Fab (PDB 7XSW) were used. The initial models were rigid body docked into the density map using UCSF Chimera's "fit to map" tool and combined. The Fab CDR loops were manually fitted to the density map using Coot real space refinement. The models were fit to density using the ISOLDE package in ChimeraX[77]. Ramachandran outliers were corrected using ISOLDE's "flip peptide bond" feature. Real space refinement in Phenix[78] was performed to remove geometry outliers. The remaining manual adjustments were performed in Coot. Models were validated using MolProbity16 in Phenix and the PDB validation server and deposited to the PDB with accession codes: 19-77+SARS-CoV-2 D614G RBD (PDB 9CFE), 19-77+HK.3 RBD (PDB 9CFF), 19-77ΔV+HK.3 RBD (PDB 9CFG), and 19-77ΔV+JD.1.1 RBD (PDB 9CFH). A summary of data collection, processing, and model refinement statistics is shown in **Figure S2**.

In silico antibody engineering

The energy changes for the binding of both the mutant and original 19-77 to the HK.3 RBD were calculated using FoldX software[38]. Initially, the 19-77 and HK.3 complex was repaired and optimized using the 'Optimize' function. Subsequently, every position in the heavy and light chains was subjected to saturation mutagenesis to all other amino acids using the 'BuildModel' function. This process generated both an unmutated model and a mutant model for each mutation. The binding energies were estimated with the 'AnalyseComplex' function, and the changes in Gibbs free energy (ΔΔG) were calculated based on the energy difference between each mutant and its corresponding original antibody-RBD complex.

Molecular dynamics analysis

Antibody 19-77, along with other VH3-53/66 class antibodies, was meticulously aligned through the RBD within each complex to ensure structural consistency. The R71A mutant antibodies were precisely engineered using the 'Mutagenesis' function in PyMOL version 2.5.4, provided by Schrödinger, LLC. Subsequently, the Fab regions of both the original and mutant

1236 antibodies underwent molecular dynamics simulations employing GROMACS on the WebGro
1237 server. The preprocessing was executed using the GROMOS96 54a7 force field and
1238 incorporated an SPC water model within a cubic simulation box, supplemented with 0.15M
1239 NaCl to mimic physiological ionic strength. The initial energy minimization step was set to
1240 5000 iterations to stabilize the system. This was followed by equilibration and simulation
1241 phases under NVT/NPT conditions, conducted at a physiological temperature of 310K for 10
1242 ns, with all other parameters set to default. To ensure the reliability of the simulation, the root-
1243 mean-square deviation (RMSD) of each system was manually monitored to verify that each
1244 simulation reached equilibrium. Additionally, the per-residue root-mean-square fluctuation
1245 (RMSF) analysis was conducted to assess the flexibility of residues within each Fab region.
1246
1247 **Structure comparison analysis**
1248 The paratope and epitope residues for 19-77 was identified using PISA with the default
1249 parameters. The gene-specific substitution profiles (GSSP) for 19-77 germline genes were
1250 obtained from the cAb-Rep database (https://cab-rep.c2b2.columbia.edu/). The 19-77 and its
1251 mutant complexes were first superimposed by using the 'align' function in PyMOL 2.5.4. The
1252 distance between the Cα from identical residues within the 19-77 heavy chains were then
1253 determined using the rms_cur function in PyMOL by in house python script.
1254
1255 **QUANTIFICATION AND STATISTICAL ANALYSIS**
1256 IC_{50} and ID_{50} values were determined by fitting the data to five-parameter dose-response curves
1257 in GraphPad Prism v.10.